Journal of Computational and Applied Mathematics 236 (2012) 3319–3337

Contents lists available at SciVerse ScienceDirect

Journal of Computational and Applied Mathematics

journal homepage: www.elsevier.com/locate/cam

Finite element boundary value integration of Wheeler–Feynman electrodynamics

Jayme De Luca [a], A.R. Humphries [b], Savio B. Rodrigues [c,*]

[a] Departamento de Física, Universidade Federal de São Carlos, São Carlos, São Paulo 13565-905, Brazil

[b] Department of Mathematics and Statistics, McGill University, Montreal, Quebec, H3A 2K6, Canada

[c] Departamento de Matemática, Universidade Federal de São Carlos, São Carlos, São Paulo 13565-905, Brazil

ARTICLE INFO

Article history:
Received 8 November 2010
Received in revised form 28 December 2011

Keywords:
Wheeler–Feynman electrodynamics
State-dependent delay
Mixed-type neutral equations
Variational method
Finite element method

ABSTRACT

The electromagnetic two-body problem is solved as a boundary value problem associated to an action functional. We show that the functional is Fréchet differentiable and that its conditions for criticality are the mixed-type neutral differential delay equations with state-dependent delay of Wheeler–Feynman electrodynamics. We construct a finite element method that finds C^1-smooth solutions when suitable past and future positions of the particles are given as boundary data. The numerical trajectories satisfy a variational problem defined in a finite-dimensional Hermite functional space of C^1 piecewise-polynomials. The numerical variational problem is solved using a combination of Newton's method intercalated with boundary adjustments to ensure that the velocity of the solution is continuous with the boundary data. We recover the known circular orbits and compute several other novel trajectories of the Wheeler–Feynman electrodynamics. We also discuss the local convexity of the functional close to the new found trajectories and the possibility of solutions with less regularity.

© 2012 Elsevier B.V. All rights reserved.

1. Introduction

The Fokker action functional is a synthetic principle of electrodynamics discovered in the early 20th century [1,2] and used in 1945 by Wheeler and Feynman [3] to construct an alternative description of classical electromagnetism that avoids the notion of field. Wheeler–Feynman electrodynamics describes point charges moving without self-interaction and interacting in pairs with the half-retarded plus half-advanced solutions of Maxwell's equations [4]. The equations for two-body motion of the Wheeler–Feynman theory are state-dependent mixed-type neutral differential-delay equations and little is known about solutions. There exists a one-parameter family of circular-orbit solutions [5,6], and an existence result for globally C^2 orbits with repulsive interaction and initial conditions restricted to collinear orbits [7]. An existence result for non co-linear solutions is presented in [8]. Solutions for more than two charges are discussed in [9]. The stability of circular orbits was first studied in [10] and later in [11]. The physics of action-at-a-distance is discussed in [12,13] and some mathematics of the electromagnetic equations with deviating arguments was studied in [14–16].

We will numerically solve the (Wheeler–Feynman) mixed-type neutral differential-delay equations of motion of the electromagnetic two-body problem in three space dimensions as a boundary value problem. We use a variational formulation where the equations of motion are the condition for a critical point of a functional S. The detailed definition of S is postponed until Section 2 (see (12)). To fix ideas, we introduce the functional with the interaction terms expressed

* Corresponding author. Tel.: +55 16 3351 8220.
E-mail addresses: deluca@df.ufscar.br (J. De Luca), tony.humphries@mcgill.ca (A.R. Humphries), savio@dm.ufscar.br (S.B. Rodrigues).

0377-0427/$ – see front matter © 2012 Elsevier B.V. All rights reserved.
doi:10.1016/j.cam.2012.02.039

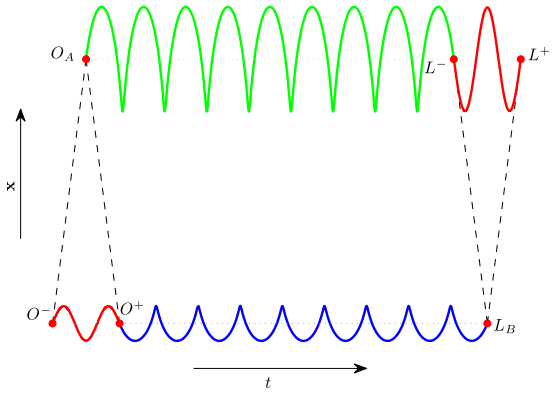


Fig. 1. A schematic showing a postulated orbit $(\boldsymbol{x}_1(t_1), \boldsymbol{x}_2(t_2))$ for $t_1 \in [t_{O_A}, t_{L^-}]$ and $t_2 \in [t_{O^+}, t_{L_B}]$ and the boundary conditions which consist of (a) the initial point $O_A = \boldsymbol{x}_1(t_{O_A})$ of the trajectory $\boldsymbol{x}_1(t_1)$ of particle 1 and the boundary segment $\boldsymbol{x}_2(t_2)$ for $t_2 \in [t_{O^-}, t_{O^+}]$ of particle 2 inside the light-cone of O_A, and (b) the final point $L_B = \boldsymbol{x}_2(t_{L_B})$ of the trajectory of particle 2 and the boundary segment $\boldsymbol{x}_1(t_1)$ for $t_1 \in [t_{L^-}, t_{L^+}]$ of particle 1 inside the light-cone of L_B.

as an integral over the time of particle 1,

$$S = -m_1 \int_{t_{O_A}}^{t_{L^-}} \sqrt{\langle \dot{\boldsymbol{x}}_1 \cdot \dot{\boldsymbol{x}}_1 \rangle} dt_1 - m_2 \int_{t_{O_A}}^{t_{L^-}} \sqrt{\langle \dot{\boldsymbol{x}}_2 \cdot \dot{\boldsymbol{x}}_2 \rangle} dt_2 + \int_{t_{O_A}}^{t_{L^+}} \frac{\langle \dot{\boldsymbol{x}}_1 \cdot \dot{\boldsymbol{x}}_{2-} \rangle}{2\langle (\boldsymbol{x}_1 - \boldsymbol{x}_{2-}) \cdot \dot{\boldsymbol{x}}_{2-} \rangle} dt_1 + \int_{t_{O_A}}^{t_{L^-}} \frac{\langle \dot{\boldsymbol{x}}_1 \cdot \dot{\boldsymbol{x}}_{2+} \rangle}{2\langle (\boldsymbol{x}_{2+} - \boldsymbol{x}_1) \cdot \dot{\boldsymbol{x}}_{2+} \rangle} dt_1, \tag{1}$$

where $\boldsymbol{x}_1(t_1)$ and $\boldsymbol{x}_2(t_2)$ are the trajectories of the two particles in four-dimensional space–time. These trajectories are parametrized respectively by the time t_1 of particle 1 (trajectory 1) and the time t_2 of particle 2 (trajectory 2). The notation $\langle \boldsymbol{x}_i \cdot \boldsymbol{x}_j \rangle$ represents a bilinear form: the Minkowski vector product (defined below in Eq. (2)). The first two integrals are the "relativistic kinetic energies"; the last two integrals represent the attractive electromagnetic interactions occurring when particle 2 is at the light-cone of trajectory 1. The sub-index $+$ and $-$ indicate the two advanced and retarded times $t_{2\pm}$ where particle 2 crosses the light-cone of particle 1; thus, $t_{2\pm}(t_1; \boldsymbol{x}_1, \boldsymbol{x}_2)$ are implicit functions of t_1 which also depend on the trajectories $\boldsymbol{x}_1$ and $\boldsymbol{x}_2$ (see (3) and (7)).

The functional S is defined for trajectories that are C^1 with acceleration existing almost everywhere. The functional also needs to be defined with suitable boundary conditions in order to provide data for the advanced and retarded arguments. Here we use the boundary conditions recently developed in [17] and illustrated in Fig. 1; they consist of (a) the initial point for trajectory 1 and the respective boundary-segment of trajectory 2 inside the light-cone of this initial point, and (b) the final point for the trajectory of particle 2 and the respective boundary-segment of trajectory 1 inside its light-cone. The mathematical problem is to *find* the two unknown segments of trajectories between the given endpoints (in Fig. 1 the endpoints are: O_A, O^+, L^-, and L_B).

The Wheeler–Feynman Equations (WFEs) of motion of the electromagnetic two-body problem follow from the condition for a critical point of the functional, provided trajectories and boundary segments are C^1 with acceleration defined almost everywhere and with velocities that match continuously to boundary segments (Fig. 1), and so we will restrict attention to trajectories of this type. The regularity of trajectories is not expected to be better than C^1 in general. Accelerations are generically discontinuous at boundary points and, since the force at one particle depends on the acceleration of the other, acceleration discontinuities propagate through sewing chains of breaking points connected by light-cones. Even just to obtain C^1 regularity we require the *splicing condition* that the velocity of the solution match continuously to the velocity of the boundary segment (see Section 2). This imposes an implicit condition on the allowable boundary data, which cannot be determined *a priori*, except in special cases. One such special case is boundary data corresponding to the known C^∞ Schönberg–Schild circular-orbit solutions [5,6].

The electromagnetic two-body problem of Wheeler–Feynman is extraordinarily challenging to solve numerically because of the combination of difficulties it presents. As a functional differential equation it presents both *advanced* and retarded arguments, making it unsuitable for direct integration as an initial value problem. Additionally in three space dimensions the functional differential equation is of *neutral* type, and the equations are always *stiff* in the sense of numerical analysis. Finally, the state dependency of the advanced and delayed terms is *implicit*; the length of the delay depends not only on the current state of the system, but also on the state at the delayed time. Despite these difficulties, a number of attempts have been made to numerically integrate the electromagnetic two-body problem [18–20]. All of these works remove the advanced term from the equations using different arguments (symmetry in [18], assumed periodicity in [20]) so that they can be numerically integrated as initial value problems. Additionally they only treat the case of motion in one or two space dimensions, which avoids the neutrality of the delay differential equations in three space dimensions.

Even formulated as a boundary value problem, it is not possible to solve the equations numerically with a standard boundary value problem software because of the advanced and delayed arguments, most of such software being developed for ordinary differential equations. Two numerical codes which do treat state-dependent delay differential boundary value problems are DDE-BIFTOOL [21] and COLDLY [22], but DDE-BIFTOOL does not allow advanced arguments, and neither code allows implicitly state-dependent delays as arising in the electromagnetic two-body problem.

In Section 2, we explain the variational formulation of the WFEs and the derivation of the functional S in some detail. These details are needed, because in Section 3 we develop a new numerical method for the WFEs based on this variational formulation of the critical point of the functional S. Since we have a variational formulation it is natural to use the finite-element method to compute the solution as the critical point of the functional in a finite-element space of C^1 trajectories satisfying suitable boundary conditions. The finite-dimensional function space we use consists of C^1 functions that are piecewise cubic polynomials between numerical grid points with both position and velocity defined at each time grid point (the Hermite function space H^2_Δ [23]). This function space enforces C^1 continuity of the numerical solution with an acceleration which is piecewise linear between grid points, and allows the numerical solution to capture the discontinuities in the acceleration at the breaking points.

The finite-element approximation leads to a non-linear algebraic system of equations which we solve using Newton's method; Jacobians are approximated by finite-differences. For arbitrary boundary data, it is not possible to guarantee *a priori* that the solution will satisfy the velocity splicing condition at the boundaries. Nevertheless, the splicing condition is necessary to show that Wheeler–Feynman equations of motion hold everywhere along a trajectory that is a critical point of the Fokker-like functional, and so we need to select boundary data on which the splicing condition can be satisfied. We do this iteratively. Our finite element method allows free velocities at endpoints of the computation and so typically converges to C^1 orbits but with discontinuous velocities at the boundaries with the boundary segments. The boundary segment is then adjusted iteratively to remove the discontinuity in the velocity (by adding it to a suitable polynomial, as detailed in Section 3).

In Section 4, we show numerical experiments, discuss the precision of the numerical method and describe new solutions of the WFEs of motion. We divide these experiments into two classes: experiments with the known Schönberg–Schild circular orbits [5,6] and experiments with new orbits. In the case of boundary data corresponding exactly to a circular-orbit solution our numerical method accurately recovers the known solution, and we use this problem to confirm the convergence order of the numerical method.

New solutions of the WFEs emerge when we consider boundaries that are different from circular orbits. In Section 4, we report on three new type of orbits which we have found, by taking boundary data based on deformations of segments of circular-orbit solutions. We find new solutions from perturbed circular boundaries, which are either close to circular solutions or surprisingly far from them. In every solution, we observe that the numerical convergence of the boundary iterative procedure is very robust.

In Section 4, we also research the convexity properties of S in different ways. In [17], a local convexity result is proven, i.e., that a circular orbit is a local minimum when the radius of the orbit is large enough. We find numerical evidence indicating that circular orbits are local minima even if the radius is not large. We also find numerical examples of non-circular orbits that are saddle points of S. Moreover, starting close to a saddle point solution, our numerical method converges to a surprising new non-circular solution which is a local minimum of S, providing numerical evidence for the existence of a bifurcation. In Section 5, we summarize and discuss our results.

2. Variational method

We define an action on a Lorentz four-space $\mathcal{L}^4$ attached to an inertial frame by Einstein synchronization of clocks. A point in $\mathcal{L}^4$ is defined by a time t and a spatial position $\mathbf{x}$, i.e., $\boldsymbol{x}^\mu \equiv (t, \mathbf{x})$, henceforth called the time-component t and the three-vector spatial component $\mathbf{x}$. The index μ belongs to $(1, 2, 3, 4)$, with $\mu = 1$ denoting the time-component while $\mu = 2, 3, 4$ denote the spatial components. We define the dual of a four-vector $\boldsymbol{x}^\mu = (t, \mathbf{x})$ by $\boldsymbol{x}_\mu \equiv (t, -\mathbf{x})$. To abbreviate notation we omit the upper index and write simply $\boldsymbol{x}$ for $\boldsymbol{x}^\mu$, while the Minkowski-dual-vector $\boldsymbol{x}_\mu$ is indicated by $\boldsymbol{x}^\dagger$. Thus $\boldsymbol{x} = (t, \mathbf{x})$, with the three-vector $\mathbf{x}$ and four vector $\boldsymbol{x}$ notationally differentiated only by the typeface used (but we note that in the sequel $\mathbf{x}$ will be parametrized by t so $\boldsymbol{x}(t)$ will be trivially isomorphic to $\mathbf{x}(t)$). We identify the four-vectors with vectors of $\mathbb{R}^4$ and use a vertical bar to denote the usual scalar product of $\mathbb{R}^4$, i.e., $\langle \boldsymbol{x} | \boldsymbol{y} \rangle \equiv x_1y_1 + x_2y_2 + x_3y_3 + x_4y_4$. The Minkowski product is a bilinear product defined as the scalar product on $\mathbb{R}^4$ between the first vector and the second vector's dual (or vice-versa), i.e.,

$$\langle \boldsymbol{x} \cdot \boldsymbol{y} \rangle \equiv x_1y_1 - x_2y_2 - x_3y_3 - x_4y_4 = \langle \boldsymbol{x} | \boldsymbol{y}^\dagger \rangle = \langle \boldsymbol{x}^\dagger | \boldsymbol{y} \rangle. \tag{2}$$

For notational convenience only, whenever $\langle \boldsymbol{x} \cdot \boldsymbol{x} \rangle \geq 0$ (so-called time-like vectors) we define $|\boldsymbol{x}|^2 \equiv \langle \boldsymbol{x} \cdot \boldsymbol{x} \rangle$, but note that $|\boldsymbol{x}|$ thus defined is not a norm. The Euclidean $\mathbb{R}^3$ norm of the spatial three-vector part of a four-vector is indicated by double bars, i.e., $\|\mathbf{x}\|$. We also use double bars to indicate the absolute value of a real number, while the Euclidean norm on $\mathbb{R}^4$ of the $\mathbb{R}^4$-image of a four-vector is indicated by double bars with sub-index 4, i.e., $\|\boldsymbol{a}\|_4$.

Each trajectory $\boldsymbol{x}_i(t_i) : \mathbb{R} \to \mathbb{R}^4$ is parametrized by time t_i, with lower index $i \in (1, 2)$ indicating the electronic and protonic trajectories respectively. We normalize the speed of light to be $c \equiv 1$, and require all trajectories to be *subluminal*, i.e., the speed is less then the speed of light at all times, which is expressed by $\langle \dot{\boldsymbol{x}}_i \cdot \dot{\boldsymbol{x}}_i \rangle \geq 0$, or equivalently $\|\dot{\mathbf{x}}_i\| < 1$.

The boundary conditions are illustrated in Fig. 1 and consist of

(a) the initial point $O_A = (t_{O_A}, \mathbf{O}_A) = \boldsymbol{x}_1(t_{O_A})$ of trajectory 1 and the respective segment of trajectory 2, (henceforth called the *boundary segment*) inside the light-cone of O_A, namely for $t_2 \in [t_{O^-}, t_{O^+}]$. The points $\boldsymbol{x}_1(t_1 = t_{O_A})$ and $\boldsymbol{x}_2(t_2 = t_{O^\pm})$ satisfy the light-cone condition

$$|\boldsymbol{x}_1(t_1) - \boldsymbol{x}_2(t_2)|^2 = 0, \tag{3}$$

(b) and, the final point $L_B = (t_{L_B}, \mathbf{L}_B) = \boldsymbol{x}_2(t_{L_B})$ of trajectory 2 and the respective boundary segment of trajectory 1 inside the light-cone of L_B, namely for $t_1 \in [t_{L^-}, t_{L^+}]$ where $\boldsymbol{x}_2(t_1 = t_{L_B})$ and $\boldsymbol{x}_1(t_1 = t_{L^\pm})$ satisfy the light-cone condition (3).

We assume that the segments of trajectory falling in the light-cones in (a) and (b) are C^1. Consistent boundary data must be such that the linear trajectories connecting $\boldsymbol{x}_1(t_{O_A})$ to $\boldsymbol{x}_1(t_{L^-})$ and $\boldsymbol{x}_2(t_{O^+})$ and to $\boldsymbol{x}_2(t_{L_B})$ are subluminal, otherwise it will be impossible to construct subluminal solutions to our boundary value problem. Besides, the future light-cone of point O^+ must fall along trajectory 1 at a time before t_{L^-}, so that the past and future histories do not interact. A more subtle restriction on the boundary data to enforce a so-called *splicing condition* will also arise naturally below.

In the following lemma, we show that for each subluminal pair of trajectories, given a four position $\boldsymbol{x}_1$ along trajectory 1, there exists exactly one delayed-time, $t_{2-}(\boldsymbol{x}_1)$, and exactly one advanced-time, $t_{2+}(\boldsymbol{x}_1)$, satisfying the lightcone condition (3).

Lemma 1. *Given C^1-smooth subluminal trajectories $\boldsymbol{x}_1(t_1)$ and $\boldsymbol{x}_2(t_2)$, that do not collide and satisfy the boundary conditions* (a) *and* (b)*, then*

(i) *the light-cone condition (3) defines exactly two implicit functions, $t_{2+}(\boldsymbol{x}_1)$ and $t_{2-}(\boldsymbol{x}_1)$, with $t_{2+} > t_1$ and $t_{2-} < t_1$ respectively;*

(ii) *these functions are C^1 functions of $\boldsymbol{x}_1 \in \mathbb{R}^4$ with derivative given by*

$$\frac{\partial t_{2\pm}}{\partial \boldsymbol{x}_1} = \frac{\boldsymbol{x}^\dagger_{12\pm}}{\langle \boldsymbol{x}^\dagger_{12\pm} | \dot{\boldsymbol{x}}_{2\pm} \rangle}, \tag{4}$$

where the derivative is taken with the Euclidean norm of $\mathbb{R}^4$ and the following notation is used:

$$\boldsymbol{x}_{2\pm} \equiv \boldsymbol{x}_2(t_{2\pm}(t_1)), \qquad \dot{\boldsymbol{x}}_{2\pm} \equiv \dot{\boldsymbol{x}}_2(t_{2\pm}(t_1)), \qquad \boldsymbol{x}_{12\pm} \equiv \boldsymbol{x}_1 - \boldsymbol{x}_{2\pm}; \tag{5}$$

(iii) *the denominators of functional (1) never vanish, i.e., $\langle \boldsymbol{x}^\dagger_{12\pm} | \dot{\boldsymbol{x}}_{2\pm} \rangle \neq 0$.*

Proof. To prove (i), we introduce functions $f_\pm(t_1, t_2) \equiv t_1 - t_2 \pm \|\mathbf{x}_1(t_1) - \mathbf{x}_2(t_2)\|$; and observe that $f_\pm = 0$ is equivalent to the lightcone condition (3). First we prove that $f_\pm$ are monotonic increasing in the first argument and monotonic decreasing in the second argument. The derivative is $\partial f_\pm / \partial t_1 = \langle (1, \dot{\mathbf{x}}_1) \cdot (1, \mp \hat{\mathbf{n}}) \rangle$, where $\|\hat{\mathbf{n}}\| = 1$ is a unitary vector. Since the orbit is subluminal, $\|\dot{\mathbf{x}}_1\| < 1$, it follows that $\partial f_\pm / \partial t_1 > 0$. Analogous calculation shows that $\partial f_\pm / \partial t_2 < 0$. From the monotonicity of the first argument, it follows that $f_-(t_1, t_{O^-}) > 0$ and $f_-(t_1, t_{L_B}) < 0$ for every $t_1 \in (t_{O_A}, t_{L^+})$ because the boundary conditions (a) and (b) impose that $f_-(t_{L^+}, t_{L_B}) = 0$ and $f_-(t_{O_A}, t_{O^-}) = 0$. Since f_- is monotonically decreasing in the second argument, we conclude that there is a unique $t_{2-} \in (t_{O^-}, t_{L_B})$ such that $f_-(t_1, t_{2-}) = 0$. Analogous argument shows the existence of a unique solution for $f_+(t_1, t_{2+}) = 0$ within the intervals $t_1 \in (t_{O_A}, t_{L^-})$ and $t_{2-} \in (t_{O^+}, t_{L_B})$. The proof of (ii) follows from implicit differentiation of the lightcone condition (3) conveniently expressed as $\langle \boldsymbol{x}^\dagger_{12\pm} | \boldsymbol{x}_{12\pm} \rangle = 0$. The C^1 smoothness follows from the Implicit Function Theorem and (iii). Finally, (iii) follows because

$$\langle \boldsymbol{x}^\dagger_{12\pm} | \dot{\boldsymbol{x}}_{2\pm} \rangle = t_1 - t_{2\pm} - \|\mathbf{x}_1(t_1) - \mathbf{x}_2(t_{2\pm})\| \, \|\dot{\mathbf{x}}_2(t_{2\pm})\| \cos\theta, \tag{6}$$

where $\|\dot{\mathbf{x}}_2(t_{2\pm})\| < 1$, and $\|t_1 - t_{2\pm}\| = \|\mathbf{x}_1(t_1) - \mathbf{x}_2(t_{2\pm})\|$ by the light-cone condition, which is nonzero as the orbits do not intersect. □

In view of the preceding lemma, we can cast (3) in an equivalent form

$$t_{2\mp} = t_1 \mp \|\mathbf{x}_2(t_{2\mp}) - \mathbf{x}_1(t_1)\|, \tag{7}$$

or in an analogous formula with the roles of t_1 and t_2 interchanged. As a result, along a subluminal and noncollisional orbit there are four advanced or retarded parametrization maps:

$$t_1 \to t_{2+}(t_1, \mathbf{x}_1(t_1)), \qquad t_1 \to t_{2-}(t_1, \mathbf{x}_1(t_1)), \qquad t_2 \to t_{1+}(t_2, \mathbf{x}_2(t_2)), \qquad t_2 \to t_{1-}(t_2, \mathbf{x}_2(t_2)), \tag{8}$$

which define the quantities in (5) and

$$\boldsymbol{x}_{1\pm} \equiv \boldsymbol{x}_1(t_{1\pm}(t_2)), \qquad \dot{\boldsymbol{x}}_{1\pm} \equiv \dot{\boldsymbol{x}}_1(t_{1\pm}(t_2)), \qquad \boldsymbol{x}_{21\pm} \equiv \boldsymbol{x}_2 - \boldsymbol{x}_{1\pm}. \tag{9}$$

To change the integration variable on the interaction integrals we shall need the derivative of the delayed times $t_{2\pm}(t_1, \mathbf{x}_1(t_1))$ taken along the orbit, which by use of (4) is

$$\frac{dt_{2\pm}}{dt_1} = \frac{\langle \boldsymbol{x}^\dagger_{12\pm} | \dot{\boldsymbol{x}}_1 \rangle}{\langle \boldsymbol{x}^\dagger_{12\pm} | \dot{\boldsymbol{x}}_{2\pm} \rangle}. \tag{10}$$

We will use the Fokker-like action with definite integrals introduced in [17] for sub-luminal and non-collisional trajectories consistent with the boundary conditions (a) and (b). Using a normalized unit system where the electronic and protonic mass and charge are m_1 and $e_1 = -1$ and m_2 and $e_2 = 1$ respectively, let

$$K_i \equiv -m_i\sqrt{\langle \dot{\boldsymbol{x}}_i \cdot \dot{\boldsymbol{x}}_i\rangle}, \qquad U_{ij}^{\pm}(\boldsymbol{x}_i, \boldsymbol{x}_{j\pm}, \dot{\boldsymbol{x}}_i, \dot{\boldsymbol{x}}_{j\pm}) \equiv -\frac{\langle \dot{\boldsymbol{x}}_i \cdot \dot{\boldsymbol{x}}_{j\pm}\rangle}{2\|\langle \boldsymbol{x}_{ij\pm} \cdot \dot{\boldsymbol{x}}_{j\pm}\rangle\|} \tag{11}$$

where $i = 1, 2$ and $j = 3 - i$. Then, due to parametrization invariance, the action can be defined in two equivalent ways as:

$$\begin{aligned} S &= \int_{t_{O_A}}^{t_{L^-}} K_1 dt_1 + \int_{t_{O^+}}^{t_{L_B}} K_2 dt_2 - \underbrace{\int_{t_{O_A}}^{t_{L^+}} U_{12}^{-} dt_1}_{\|} - \underbrace{\int_{t_{O_A}}^{t_{L^-}} U_{12}^{+} dt_1}_{\|} \\ &= \int_{t_{O_A}}^{t_{L^-}} K_1 dt_1 + \int_{t_{O^+}}^{t_{L_B}} K_2 dt_2 - \overbrace{\int_{t_{O^-}}^{t_{L_B}} U_{21}^{+} dt_2} - \overbrace{\int_{t_{O^+}}^{t_{L_B}} U_{21}^{-} dt_2}, \end{aligned} \tag{12}$$

where dot denotes a derivative respect to the time of each trajectory. The positions and velocities for $t_1 \in [t_{L^-}, t_{L^+}]$ and $t_2 \in [t_{O^-}, t_{O^+}]$ are given by the respective boundary segments. One can verify that the two expressions for S are equivalent by changing the integration variable from t_2 to t_1 using (10). Eq. (1) for S can be derived by inspecting the signs of $\langle \boldsymbol{x}_{ij\pm} \cdot \dot{\boldsymbol{x}}_{j\pm}\rangle$ in the denominator of $U_{ij}^{\pm}$ to remove the absolute values. We remark that the denominator never vanishes by Lemma 1(iii). Since there are two different ways to express the electromagnetic functional, each choice of the integration variable defines a *different* integrand (i.e., a different Lagrangian for each particle). This fact is unseen in Galilei-invariant two-body actions, and is worth stressing. Notice that in (1) the trajectory of particle 2 is to be kept fixed while we take the linear variation respect to trajectory 1, i.e., all non-constant integrals in Eq. (1) are over the time of particle 1. This splitting in two different *partial Lagrangians*, each with the other particle's trajectory frozen, is the most convenient way to work out the general linear variation by adding the two partial variations to make the Fréchet derivative.

Having shown that S is well defined along a sub-luminal non-collisional orbit, we now discuss its differentiation. In the following we prove Fréchet differentiability in a neighborhood of each sub-luminal non-collisional orbit, which will be sufficient for our purposes, but is weaker than Fréchet differentiability on the whole Banach space.

Let $(\boldsymbol{x}_{1L}(t_1), \boldsymbol{x}_{2L}(t_2))$ be a C^1 reference orbit which satisfies the boundary conditions (a) and (b) but not (necessarily) either the splicing condition or the equations of motion; for example it could be the linear trajectories between the boundary conditions, or a guess for the solution. Then the vector space of C^1 orbital-perturbations $(\boldsymbol{b}_1(t_1), \boldsymbol{b}_2(t_2))$ is denoted by $N(\boldsymbol{x}_{1L}, \boldsymbol{x}_{2L})$ which induces the affine space $M(\boldsymbol{x}_{1L}, \boldsymbol{x}_{2L})$ of trajectories $(\boldsymbol{u}_1, \boldsymbol{u}_2)$ defined by

$$\boldsymbol{u}_1 \equiv \boldsymbol{x}_{1L} + \boldsymbol{b}_1, \qquad \dot{\boldsymbol{u}}_1 \equiv \dot{\boldsymbol{x}}_{1L} + \dot{\boldsymbol{b}}_1, \tag{13}$$

where $\boldsymbol{b}_1(t_1)$ vanishes at endpoints in accordance with

$$\boldsymbol{b}_1(t_1 = t_{O_A}) = \boldsymbol{b}_1(t_1 = t_{L^-}) = 0, \tag{14}$$

and

$$\boldsymbol{u}_2 \equiv \boldsymbol{x}_{2L} + \boldsymbol{b}_2, \qquad \dot{\boldsymbol{u}}_2 \equiv \dot{\boldsymbol{x}}_{2L} + \dot{\boldsymbol{b}}_2, \tag{15}$$

where $\boldsymbol{b}_2$ vanishes at endpoints in accordance with

$$\boldsymbol{b}_2(t_2 = t_{O^+}) = \boldsymbol{b}_2(t_2 = t_{L_B}) = 0. \tag{16}$$

The boundary conditions (a) and (b) specify a *unique* Lorentz frame, so that we cannot apply a Lorentz transformation to $\boldsymbol{b}_1(t_1)$ without destroying (14) and (16), which could otherwise be done using the Lorentz-invariance of the action. Therefore, for any given time t we can identify the space of the $\boldsymbol{b}_1(t)$ with $\mathbb{R}^4$, which is a complete normed space with the usual Euclidean norm of $\mathbb{R}^4$. It is important to distinguish two linear spaces used here. (i) For any given time $t_1 \in [t_{O_A}, t_{L^+}]$, $\boldsymbol{b}_1(t_1)$ is in $\mathbb{R}^4$ which is a finite-dimensional space, while (ii) the set of C^1 orbits defined by $\boldsymbol{b}_1(t) : [t_{L^-}, t_{L^+}] \to \mathbb{R}^4$ satisfying (14) and (16) forms an infinite-dimensional Banach space. As discussed in [17], the above defined trajectory space $N(\boldsymbol{x}_{1L}, \boldsymbol{x}_{2L})$ is a Banach space with norm

$$|\boldsymbol{b}_1, \boldsymbol{b}_2|_{N(x_{1L}, x_{2L})} \equiv \sum_{i=1}^{2} \sup \|\boldsymbol{b}_i\|_4 + \sup \|\dot{\boldsymbol{b}}_i\|_4. \tag{17}$$

It will be useful later to note that the space $N(\boldsymbol{x}_{1L}, \boldsymbol{x}_{2L})$ can be viewed as the direct sum of two subspaces, $N(\boldsymbol{x}_{1L}, \boldsymbol{x}_{2L}) = N_1 \oplus N_2$, where $\boldsymbol{b}_2 = 0$ and $\boldsymbol{b}_1 = 0$ respectively in each subspace.

In Theorem 2, we prove that the functional S is Frechét differentiable for a C^1 trajectory variation which is piecewise C^2 with a second derivative defined almost everywhere. The trajectory perturbation $\boldsymbol{u}_k \to \boldsymbol{x}_k + \boldsymbol{b}_k$ about the piecewise C^2

orbit $(\boldsymbol{x}_1(t_1), \boldsymbol{x}_2(t_2))$ induces a variation δS which has the form

$$\delta S = \int_{t_{O_A}}^{t_{L^-}} \left\langle \frac{\partial K_1}{\partial \dot{\boldsymbol{x}}_1} \middle| \dot{\boldsymbol{b}}_1 \right\rangle dt_1 + \int_{t_{O^+}}^{t_{L_B}} \left\langle \frac{\partial K_2}{\partial \dot{\boldsymbol{x}}_2} \middle| \dot{\boldsymbol{b}}_2 \right\rangle dt_2 - \int_{t_{O_A}}^{t_{L^-}} \left\langle \frac{\partial U_{12}^-}{\partial \boldsymbol{x}_1} \middle| \boldsymbol{b}_1 \right\rangle - \left\langle \frac{\partial U_{12}^-}{\partial \dot{\boldsymbol{x}}_1} \middle| \dot{\boldsymbol{b}}_1 \right\rangle dt_1 - \int_{t_{O_A}}^{t_{L^-}} \left\langle \frac{\partial U_{12}^+}{\partial \boldsymbol{x}_1} \middle| \boldsymbol{b}_1 \right\rangle$$
$$- \left\langle \frac{\partial U_{12}^+}{\partial \dot{\boldsymbol{x}}_1} \middle| \dot{\boldsymbol{b}}_1 \right\rangle dt_1 - \int_{t_{O^+}}^{t_{L_B}} \left\langle \frac{\partial U_{21}^-}{\partial \boldsymbol{x}_2} \middle| \boldsymbol{b}_2 \right\rangle - \left\langle \frac{\partial U_{21}^-}{\partial \dot{\boldsymbol{x}}_2} \middle| \dot{\boldsymbol{b}}_2 \right\rangle dt_2 - \int_{t_{O^+}}^{t_{L_B}} \left\langle \frac{\partial U_{21}^+}{\partial \boldsymbol{x}_2} \middle| \boldsymbol{b}_2 \right\rangle - \left\langle \frac{\partial U_{21}^+}{\partial \dot{\boldsymbol{x}}_2} \middle| \dot{\boldsymbol{b}}_2 \right\rangle dt_2. \tag{18}$$

When the derivatives $\dot{\boldsymbol{x}}_1$ and $\dot{\boldsymbol{x}}_2$ match continuously to the respective boundary segments at $t_1 = t_{L^-}$, $t_2 = t_{O^+}$, integration by parts yields

$$\delta S = \int_{t_{O_A}}^{t_{L^-}} \langle \boldsymbol{G}_1 | \boldsymbol{b}_1 \rangle dt_1 + \int_{t_{O^+}}^{t_{L_B}} \langle \boldsymbol{G}_2 | \boldsymbol{b}_2 \rangle dt_{2+} + \mathcal{O}\big(|\boldsymbol{b}_1, \boldsymbol{b}_2|^2_{N(x_{1L}, x_{2L})}\big) \tag{19}$$

where $\boldsymbol{G}_1$ and $\boldsymbol{G}_2$ are defined almost everywhere by

$$\boldsymbol{G}_1 = \frac{d}{dt_1}\left[\frac{m_1 \dot{\boldsymbol{x}}_1^\dagger}{\sqrt{\dot{\boldsymbol{x}}_1 \cdot \dot{\boldsymbol{x}}_1}} - \frac{\dot{\boldsymbol{x}}_{2+}^\dagger}{2\|\langle \boldsymbol{x}_{12+} \cdot \dot{\boldsymbol{x}}_{2+}\rangle\|} - \frac{\dot{\boldsymbol{x}}_{2-}^\dagger}{2\|\langle \boldsymbol{x}_{12-} \cdot \dot{\boldsymbol{x}}_{2-}\rangle\|}\right] + \frac{\partial}{\partial \boldsymbol{x}_1}\left[\frac{\langle \dot{\boldsymbol{x}}_1 \cdot \dot{\boldsymbol{x}}_{2+}\rangle}{2\|\langle \boldsymbol{x}_{12+} \cdot \dot{\boldsymbol{x}}_{2+}\rangle\|} + \frac{\langle \dot{\boldsymbol{x}}_1 \cdot \dot{\boldsymbol{x}}_{2-}\rangle}{2\|\langle \boldsymbol{x}_{12-} \cdot \dot{\boldsymbol{x}}_{2-}\rangle\|}\right], \tag{20}$$

and

$$\boldsymbol{G}_2 = \frac{d}{dt_2}\left[\frac{m_2 \dot{\boldsymbol{x}}_2^\dagger}{\sqrt{\dot{\boldsymbol{x}}_2 \cdot \dot{\boldsymbol{x}}_2}} - \frac{\dot{\boldsymbol{x}}_{1+}^\dagger}{2\|\langle \boldsymbol{x}_{21+} \cdot \dot{\boldsymbol{x}}_{1+}\rangle\|} - \frac{\dot{\boldsymbol{x}}_{1-}^\dagger}{2\|\langle \boldsymbol{x}_{21-} \cdot \dot{\boldsymbol{x}}_{1-}\rangle\|}\right] + \frac{\partial}{\partial \boldsymbol{x}_2}\left[\frac{\langle \dot{\boldsymbol{x}}_2 \cdot \dot{\boldsymbol{x}}_{1+}\rangle}{2\|\langle \boldsymbol{x}_{21+} \cdot \dot{\boldsymbol{x}}_{1+}\rangle\|} + \frac{\langle \dot{\boldsymbol{x}}_2 \cdot \dot{\boldsymbol{x}}_{1-}\rangle}{2\|\langle \boldsymbol{x}_{21-} \cdot \dot{\boldsymbol{x}}_{1-}\rangle\|}\right]. \tag{21}$$

The critical points for the action are the trajectories along which

$$\int_{t_{O_A}}^{t_{L^-}} \langle \boldsymbol{G}_1(t_1;\ \mathbf{x}_1, \dot{\mathbf{x}}_1, \mathbf{x}_{2+}, \dot{\mathbf{x}}_{2+}, \ddot{\mathbf{x}}_{2+}) | \boldsymbol{b}_1 \rangle dt_1 = 0, \tag{22}$$

$$\int_{t_{O^+}}^{t_{L_B}} \langle \boldsymbol{G}_2(t_2;\ \mathbf{x}_2, \dot{\mathbf{x}}_2, \mathbf{x}_{1+}, \dot{\mathbf{x}}_{1+}, \ddot{\mathbf{x}}_{1+}) | \boldsymbol{b}_2 \rangle dt_{2+} = 0, \tag{23}$$

for every $(\boldsymbol{b}_1, \boldsymbol{b}_2) \in N(\boldsymbol{x}_{1L}, \boldsymbol{x}_{2L})$, and hence the trajectories along which $\boldsymbol{G}_1 = \boldsymbol{G}_2 = 0$ almost everywhere. The conditions $\boldsymbol{G}_1 = \boldsymbol{G}_2 = 0$ along the trajectories $\boldsymbol{x}_1, \boldsymbol{x}_2$ yield the Wheeler–Feynman electromagnetic equations of motion with the Liénard–Wierchert–Lorentz force, as shown in the Appendix of [17].

Theorem 2. *The functional $S(\boldsymbol{x}_1, \boldsymbol{x}_2)$ defined in (12) is Frechét differentiable in the space $N(\boldsymbol{x}_{1L}, \boldsymbol{x}_{2L})$ when the trajectories $\boldsymbol{x}_1$ and $\boldsymbol{x}_2$ satisfy the conditions of Lemma 1.*

Proof. The proof relies on three facts: the differentiability of the functions K_i and $U_{i,j}^{\pm}$, the finite interval of integration, and statement (iii) from Lemma 1. Note that, because the integration time interval is finite, there is a minimal separation between the particles and there is a maximum speed for either particle. Thus, under the conditions of Lemma 1, there is a neighborhood of $(\boldsymbol{x}_1, \boldsymbol{x}_2)$ where S is well defined. The function K_i is differentiable because $\langle \dot{\boldsymbol{x}}_i \cdot \dot{\boldsymbol{x}}_i \rangle > 0$, and $U_{i,j}^{\pm}$ is differentiable in both of its arguments because the denominator does not vanish by Lemma 1(iii). To complete the proof that (12) is Frechét differentiable, we give a general argument that can be applied to each integral of (12). Considering a differentiable function $F(\boldsymbol{x}, \dot{\boldsymbol{x}})$, where F represents either K_i or $U_{i,j}^{\pm}$, then

$$F(\boldsymbol{x} + \boldsymbol{b}, \dot{\boldsymbol{x}} + \dot{\boldsymbol{b}}) - F(\boldsymbol{x}, \dot{\boldsymbol{x}}) - \left\langle \frac{\partial F}{\partial \boldsymbol{x}} \middle| \boldsymbol{b} \right\rangle - \left\langle \frac{\partial F}{\partial \dot{\boldsymbol{x}}} \middle| \dot{\boldsymbol{b}} \right\rangle \in \mathcal{O}((\|\boldsymbol{b}(t)\|_4 + \|\dot{\boldsymbol{b}}(t)\|_4)^2), \tag{24}$$

by force of the usual Taylor series. The integration of (24) on a *finite* time interval can be bounded by $C|\boldsymbol{b}_1, \boldsymbol{b}_2|_N^2$ and therefore (12) is Frechét differentiable. □

At this point it is worth considering further the differentiability of the solutions that we seek. In the classical Lagrangian mechanics of the two-body problem, the initial and final points define an orbit for a system of second order ODEs as a two-point boundary value problem, (i.e., the initial velocity is defined implicitly by the final point of the trajectory). In such a problem, one can replace the final point of the boundary value problem by the initial velocity and study the resulting initial value problem for a second order ODE, which must therefore have C^2 solutions. Seduced by our ODE intuition, and the presence of second derivatives in the Wheeler–Feynman equations (WFEs), it might appear natural to seek C^2 solutions of (22) and (23) subject to (a) and (b). However, in contrast to the case of classical mechanics, the differential equation corresponding to our boundary value problem, the WFEs, contain neutral state-dependent advanced and delayed arguments, and so are far from ODEs. Whether the WFEs can be well-posed as an initial value problem is a delicate question (see [15]). Moreover, in general neutrality can lead to either discontinuities or even solution termination (see [24]), although it has been

shown that termination does *not* occur for the WFEs [17]. That the boundary value problem cannot be solved for arbitrary boundary data should not come as a surprise; this is already true in the much simpler case of two-point boundary value problems for second-order ODEs. So, rather than attempting to solve the WFEs $\boldsymbol{G}_1 = \boldsymbol{G}_2 = 0$ directly, which can only be done in very special cases (see e.g. [6,20]) we will solve (22) and (23). It is then natural to solve (22) and (23) subject to (a) and (b) in $N(\boldsymbol{x}_{1L}, \boldsymbol{x}_{2L})$ with C^1 trajectories which are piecewise C^2 with a second derivative defined almost everywhere. Although the orbits will be piecewise C^2 in general, for certain special boundary conditions (e.g. the Schild orbits [6]) we expect to recover C^2 solutions.

Notice that the velocities $\dot{\mathbf{x}}_1(t_{O_A})$ and $\dot{\mathbf{x}}_2(t_{L_B})$ are arbitrary because there is no prescribed orbit either before $t_1 = t_{O_A}$ or after $t_2 = t_{L_B}$. On the other hand, $\dot{\mathbf{x}}_1(t_1)$ and $\dot{\mathbf{x}}_2(t_2)$ need to be continuous at $t_1 = t_{L^-}$ and $t_2 = t_{O^+}$ where the trajectories join the adjacent boundary segment. Continuity of velocity at these two points is essential in the integration by parts used to derive (19) from (18), otherwise some boundary related terms do not vanish and we do not recover the WFEs in (20) and (21) from the variational principle. Therefore, in order for the WFEs to be valid everywhere along the trajectories we must restrict the boundary conditions (a) and (b) with the additional condition (c).

(c) *Splicing condition*: the boundary segments defined in (a) and (b) must be such that the trajectories that solve (22) and (23) have velocities such that $\dot{\mathbf{x}}_1$ is continuous at t_{L^-} and $\dot{\mathbf{x}}_2$ continuous at t_{O^+} with respect to the boundary segments.

Conditions such as (c) are known as splicing conditions in the literature of delay differential equations, where they are used to avoid discontinuities in the velocity of neutral delay equations [24], and also to develop linearization and center and unstable manifold theory for state-dependent problems [25]. Splicing conditions for the WFEs were previously considered in [15], but whereas Murdock introduced an infinity of such conditions, we only impose a single splicing condition on $\dot{\mathbf{x}}_i$ at one point for each trajectory.

It is difficult to explicitly identify *a priori* the correct restriction of $N(\boldsymbol{x}_{1L}, \boldsymbol{x}_{2L})$ to ensure that the splicing condition (c) is satisfied. If the splicing condition is not enforced the solution of (22) and (23) will have, in general, discontinuous velocities at $t_1 = t_{L^-}$ and $t_2 = t_{O^+}$, violating hypothesis used in its derivation. In the next section, we will present an iterative technique to modify given boundary conditions to find adequate boundary-segments for which (c) holds.

We only consider the equations of motion where the splicing condition is satisfied but we refer to [26,27] for the equations resulting from the variational principle when the splicing condition is relaxed. In that case, equations (19)–(21) are no longer valid, but (18) still applies and it is possible to build a variational theory which gives rise to solutions which are piecewise C^1, with discontinuous velocity (satisfying jump-conditions) along a finite sewing chain of breaking points connected by light-cone condition, and satisfy the WFEs everywhere between the breaking points. In [26], it is shown that spatially bounded two-body orbits with far-fields vanishing almost everywhere *must* involve discontinuous velocities. Thus, solutions with discontinuous velocity would be interesting to pursue for the WFEs, though we will not do so here.

3. Numerical method

We seek critical points of the functional S (12) that are C^1 trajectories $\boldsymbol{x}_1^h(t_1)$ and $\boldsymbol{x}_2^h(t_2)$ satisfying the boundary conditions (a) and (b) and the splicing condition (c) using the Finite Element method. To do this, we define a finite-dimensional subspace $N_h(\boldsymbol{x}_{1L}, \boldsymbol{x}_{2L}) = N_{1,h_1} \oplus N_{2,h_2}$ of $N(\boldsymbol{x}_{1L}, \boldsymbol{x}_{2L})$, where N_{i,h_i} is a Hermite function space comprised of C^1-piecewise-polynomial trajectories, and we find trajectories $\boldsymbol{x}_1^h(t_1)$ and $\boldsymbol{x}_2^h(t_2)$ in this space such that (22) holds for all $\boldsymbol{b}_1 \in N_{1,h_1}$ and (23) holds for all $\boldsymbol{b}_2 \in N_{2,h_2}$. This defines a finite dimensional nonlinear system of equations which we solve using Newton's method.

In the Hermite function space used here, the value of position and velocity of the particles are defined at each interpolation point. This is a convenient feature because it forces the numerical solution to be C^1 in the computational domain, but allows the acceleration to be discontinuous at any mesh point.

We remark that satisfying the splicing condition (c) may demand adjustments of the boundary data (a) and (b). As noted in the previous section, for arbitrary C^1 boundary data, the resulting trajectories $\boldsymbol{x}_1^h(t_1)$ and $\boldsymbol{x}_2^h(t_2)$ need not in general have velocities continuous with the boundary segments at $t_1 = t_{L^-}$ and $t_2 = t_{O^+}$. Thus, if we numerically observe velocity discontinuities at $t_1 = t_{L^-}$ and $t_2 = t_{O^+}$ we need to adjust the boundary segments to remove these discontinuities. When necessary we do this iteratively as described below.

The functional S (12) is invariant under reparametrizations with a monotonic time-component, so to avoid non-unique solutions that are simply reparametrizations of each other, we discretize trajectories keeping the time variable on a fixed time-grid. Thus, given a time-grid for the trajectory of particle 1,

$$t_{O_A} = t_{1,0} < t_{1,1} < \cdots < t_{1,j} < \cdots < t_{1,M_1} = t_{L^-}, \tag{25}$$

each of the three spatial components, $\mathbf{x}_1^h = (x_1^{h,1}, x_1^{h,2}, x_1^{h,3})$, of the trajectory $\boldsymbol{x}_1^h \equiv (t_1, \mathbf{x}_1^h(t_1)) \in N_{1,h_1}$ is defined in each sub-interval by a *cubic* polynomial vector $\mathbf{P}_{1,j}(t) : [t_{1,j}, t_{1,j+1}] \to \mathbb{R}^3$, where $\mathbf{P}_{1,j}(t) = (P_{1,j}^1(t), P_{1,j}^2(t), P_{1,j}^3(t))$, is determined by Hermite interpolation conditions

$$\begin{aligned} &P_{1,j}^l(t_{1,j}) = x_{1,j}^{h,l}, \qquad \dot{P}_{1,j}(t_{1,j}) = v_{1,j}^{h,l}, \\ &P_{1,j}^l(t_{1,j+1}) = x_{1,j+1}^{h,l}, \qquad \dot{P}_{1,j}^l(t_{1,j+1}) = v_{1,j+1}^{h,l}, \end{aligned} \tag{26}$$

and where $\mathbf{x}^h_{1,j} \equiv (x^{h,1}_{1,j}, x^{h,2}_{1,j}, x^{h,3}_{1,j})$ and $\mathbf{v}^h_{1,j} \equiv (v^{h,1}_{1,j}, v^{h,2}_{1,j}, v^{h,3}_{1,j})$ are respectively the position and the velocity vector at the time-grid points $t_{1,j}$. With exception of $\mathbf{x}^h_{1,0}$ and $\mathbf{x}^h_{1,M_1}$, vectors $\mathbf{x}^h_{1,j}$ and $\mathbf{v}^h_{1,j}$ are degrees of freedom when searching for a critical point of the functional; in total, there are $6M_1$ scalar degrees of freedom for the trajectory of particle 1. The interpolation conditions impose a continuous velocity $\dot{\mathbf{x}}^h_1$ across time-grid points, while the acceleration $\ddot{\mathbf{x}}^h_1$ can be discontinuous at these points. An analogous Hermite function space N_{2,h_2} is used for trajectory $\mathbf{x}^h_2(t_2)$ on the time-grid

$$t_{O^+} = t_{2,0} < t_{2,1} < \cdots < t_{2,j} < \cdots < t_{2,M_2} = t_{L_B}, \tag{27}$$

with three-component cubic polynomials $\mathbf{P}_{2,j}(t) : [t_{2,j}, t_{2,j+1}] \to \mathbb{R}^3$, where the position, $\mathbf{x}^h_{2,j}$, and velocity, $\mathbf{v}^h_{2,j}$, are given at the time-grid points. There are $6M_2$ degrees of freedom for the trajectory of particle 2: there are 6 degrees of freedom for each time grid-point with the exception of $t_{2,0}$ and t_{2,M_2} where $\mathbf{x}^h_{2,0}$ and $\mathbf{x}^h_{2,M_2}$ are held fixed.

The Hermite function space where we seek the numerical trajectory has good approximation properties when the solution trajectory is smooth. For example, it is known [23] that if the solution trajectory of particle 1, $\boldsymbol{x}_1(t_1) \equiv (t_1, \mathbf{x}_1(t_1))$, is a C^4-smooth function and if $\mathbf{x}^h_{1,j} = \mathbf{x}_1(t_{1,j})$ and $\mathbf{v}^h_{1,j} = \dot{\mathbf{x}}_1(t_{1,j})$, then the Hermite interpolation approximates the k-th derivative with an error of $\mathcal{O}(h_1^{4-k})$, $k = 0, 1, 2$, where $h_1 = \max_j |t_{1,j+1} - t_{1,j}|$, the maximum time-grid spacing. Of course, we will not be interpolating an already known function, but will rather be using the Hermite function space to define a Finite Element basis, and also in general we do not expect the solution trajectory to be smoother than C^1, and so for both reasons these convergence rates do not apply to the numerical solution that we compute. In Experiment I of Section 4, we report on the numerical convergence rate for the smooth circular-orbit solution.

To implement the Finite Element method, we define a set of compactly-supported basis functions for the finite-dimensional space $N_h(\boldsymbol{x}_{1L}, \boldsymbol{x}_{2L})$ such that each basis function corresponds to one scalar degree of freedom of each trajectory. Since $N_h(\boldsymbol{x}_{1L}, \boldsymbol{x}_{2L}) = N_{1,h_1} \oplus N_{2,h_2}$, for each subspace N_{i,h_i}, we define a set of three-component C^1 piecewise cubic polynomial basis functions $\mathbf{B}^{k,l}_{i,j}(t_i) : [t_{i,1}, t_{i,N_i}] \to \mathbb{R}^3$, such that each trajectory $\mathbf{x}^h_i(t_i)$ can be expressed as the linear combination

$$\mathbf{x}^h_i(t_i) = \sum_{j=1}^{M_i-1} \sum_{l=1}^{3} x^{h,l}_{i,j}\, \mathbf{B}^{1,l}_{i,j}(t_i) + \sum_{j=0}^{M_i} \sum_{l=1}^{3} v^{h,l}_{i,j}\, \mathbf{B}^{2,l}_{i,j}(t_i),$$

where $x^{h,l}_{i,j}$ and $v^{h,l}_{i,j}$ are the degrees of freedom for position and velocity respectively. Using δ_{ij} to denote the Kronecker delta, the values and the derivatives of these basis functions at the grid points are

$$\begin{aligned} \mathbf{B}^{k,l}_{i,j}(t_{i,m}) &= \delta_{k1}\delta_{jm}\,(\delta_{l1}, \delta_{l2}, \delta_{l3}), \\ \dot{\mathbf{B}}^{k,l}_{i,j}(t_{i,m}) &= \delta_{k2}\delta_{jm}\,(\delta_{l1}, \delta_{l2}, \delta_{l3}). \end{aligned} \tag{28}$$

where i is the particle index ($i = 1, 2$), l is the component index ($l = 1, 2, 3,$), j is the grid point index, and k indicates if the basis-function has value one or derivative with value 1 at the grid point $t_{i,m}$ ($k = 1, 2$). As usual in the Finite Element method, the support of each basis function $\mathbf{B}^{k,l}_{i,j}(t_i)$ is within the interval $[t_{i,j-1}, t_{i,j+1}]$ when $t_{i,j}$ is not a boundary point. The value of all basis functions, and the their first derivative, vanish at the boundaries with the exception of $\mathbf{B}^{2,l}_{i,0}(t_i)$ and $\mathbf{B}^{2,l}_{i,M_i}(t_i)$, for $l = 1, 2, 3$ and $i = 1, 2$, which are linked to the velocities at the boundary points. Adding the degrees of freedom for each particle, we find the dimension of the subspace $N_h(\boldsymbol{x}_{1L}, \boldsymbol{x}_{2L})$ to be $6(M_1 + M_2)$.

A finite-dimensional nonlinear system of equations is obtained by requiring that ((22)–(23)) hold for every $(\boldsymbol{b}_1, \boldsymbol{b}_2) \in N_h(\boldsymbol{x}_{1L}, \boldsymbol{x}_{2L})$ or, equivalently, that ((22)–(23)) hold for every basis function. Eq. (22) yields a set of $6M_1$ equations:

$$0 = \mathbf{I}^{k,l}_{1,j} \equiv \int_0^{t_{L_-}} \langle \boldsymbol{G}_1(t_1;\, \mathbf{x}^h_1, \dot{\mathbf{x}}^h_1, \mathbf{x}^{h+}_2, \dot{\mathbf{x}}^{h+}_2, \ddot{\mathbf{x}}^{h+}_2) | (t_1, \mathbf{B}^{k,l}_{1,j}(t_1)) \rangle dt_1, \tag{29}$$

where $1 \le j \le M_1 - 1$ when $k = 1$, and where $0 \le j \le M_1$ when $k = 2$; $l = 1, 2, 3$. Furthermore, (23) yields a set of $6M_2$ equations:

$$0 = \mathbf{I}^{k,l}_{2,j} \equiv \int_{t_{O_+}}^{t_{L_B}} \langle \boldsymbol{G}_2(t_2;\, \mathbf{x}^h_2, \dot{\mathbf{x}}^h_2, \mathbf{x}^{h+}_1, \dot{\mathbf{x}}^{h+}_1, \ddot{\mathbf{x}}^{h+}_1) | (t_2, \mathbf{B}^{k,l}_{2,j}(t_2)) \rangle dt_2, \tag{30}$$

where $1 \le j \le M_2 - 1$ when $k = 1$, and where $0 \le j \le M_2$ when $k = 2$; $l = 1, 2, 3$.

The gradient of the functional S in the subspace $N_h(\boldsymbol{x}_{1L}, \boldsymbol{x}_{2L})$, with respect to the Finite Element basis we have chosen, is a $6(M_1 + M_2)$-dimensional vector $\nabla_h S(\mathbf{x})$ such that each of its coordinates is one of the $6(M_1 + M_2)$ scalar integrals $\mathbf{I}^{k,l}_{i,j}$ defined in (29) and (30). The order in which all the integrals $\mathbf{I}^{k,l}_{i,j}$ are arranged in $\nabla_h S(\mathbf{x})$ is arbitrary; the order influences only the sparsity pattern of the Jacobian matrix. Thus, we are using a Galerkin approximation to solve the *averaged* equations of motion ((22)–(23)) by solving $\nabla_h S = 0$ in the subspace $N_h(\boldsymbol{x}_{1L}, \boldsymbol{x}_{2L})$ (or equivalently, by requiring $\boldsymbol{G}_i$ to be orthogonal to N_{i,h_i} in the L^2-sense).

To compute the gradient $\nabla_h S(\mathbf{x}^h_1, \mathbf{x}^h_2)$, the integrals $\mathbf{I}^{k,l}_{i,j}$ are approximated using a quadrature rule on a quadrature-grid which is finer than the time-grid. Special care must be taken because the integrand is not C^n-smooth, for example, the

integrand of $\mathbf{I}_{1,j}^{k,l}$ is discontinuous either when $t_1^+ = t_{2,j}$, where $\ddot{\mathbf{x}}_2^h(t_1^+)$ has a jump discontinuity, or when $t_1 = t_{1,j}$, where $\ddot{\mathbf{x}}_1^h(t_1)$ has a jump discontinuity. To avoid these difficulties, we compute the integral $\mathbf{I}_{1,j}^{k,l}$ by applying a quadrature rule on sub-intervals $[s_{1,j}, s_{1,j+1}]$ where the integrand is C^∞-smooth; i.e., $s_{1,j}$ and $s_{1,j+1}$ are neighboring discontinuity events of the integrand that can be either a time-grid point of trajectory 1, $t_1 = t_{1,j}$, or a forward light-cone that reaches a time-grid point of trajectory 2, $t_1^+ = t_{2,j}$. Formally, for each trajectory with $i = 1, 2$, we select $s_{i,j}$ and $s_{i,j+1}$ as quadrature endpoints where

$$t_{i,0} = s_{i,1} \le \cdots \le s_{i,l} \le \cdots \le s_{i,M_1+M_2} = t_{i,N_i}, \tag{31}$$

and where either $s_{i,l} = t_{i,j}$ or $s_{i,l}^+ = t_{k,j}$; $k = 3 - i$, for $l = 1, \ldots, M_1 + M_2$. Once the integral $\mathbf{I}_{i,j}^{k,l}$ is subdivided, we apply a composite trapezoidal rule in each sub-interval $[s_{i,j}, s_{i,j+1}]$. For each evaluation of $\boldsymbol{G}_i$, the implicit relation (3) is solved to machine precision to find the light-cone that connects t_i to t_i^+. We remark that the jump discontinuities in the acceleration can remain even as h_i vanishes because the trajectory $\boldsymbol{x}_i$ may only have C^1-regularity. For sufficiently smooth trajectories or smooth parts of a trajectory, we expect these jump discontinuities to vanish as $h_i \to 0$.

The nonlinear system $\nabla_h S(\mathbf{x}_1^h, \mathbf{x}_2^h) = 0$ is solved using Newton's method, where each of the columns of the Jacobian matrix $\nabla_h^2 S$ is approximated using centered finite-differences of $\nabla_h S(\mathbf{x}_1^h, \mathbf{x}_2^h)$, resulting in an approximate Jacobian $\tilde{\nabla}_h^2 S$. Since the Jacobian matrix $\nabla_h^2 S$ is comprised of the second derivatives of S with respect to the degrees of freedom of subluminal trajectories that do not collide (and singularities are avoided in this case), the second derivatives are continuous and $\nabla_h^2 S$ is symmetric. In fact, we may call it a Hessian. The skew-symmetric part of $\tilde{\nabla}_h^2 S$ gives an indication of the numerical errors present in it; we symmetrize it to improve precision. In Section 4, a numerical example shows that the skew-symmetric part is indeed small. We remark that, with respect to the basis we have chosen, the Jacobian matrix is sparse and only the nonzero elements need to be computed; also, the entries of the gradient are ordered in a way that the Jacobian matrix becomes band-diagonal. However, the band diagonal structure is not regular due to the state-dependency of the delays, and so difficult to exploit. Hence, with an aim more towards robustness than efficiency, the sparse linear system is solved using the standard *backslash* (\) command in Matlab. We iterate Newton's method until the residual is close to zero in machine precision. For a typical initial guess, the residual is reduced by ten orders of magnitude before satisfying the precision tolerance, which requires approximately five steps of Newton's method.

Newton's method computes a sequence of approximate trajectories $\boldsymbol{x}_1^{h,j}(t_1)$ and $\boldsymbol{x}_2^{h,j}(t_2)$ for $j = 1, 2, \ldots$. If the initial guess $\boldsymbol{x}_1^{h,0}(t_1)$ or $\boldsymbol{x}_2^{h,0}(t_2)$ is far from $\boldsymbol{x}_1^h(t_1)$ or $\boldsymbol{x}_2^h(t_2)$ then the Newton updates can sometimes be very large, and cause the orbit at the jth step to be superluminal. At this point the Newton iteration would fail because the variational method is developed for subluminal orbits only. To avoid this problem we regularize Newton's method to ensure that orbits remain subluminal by first transforming the node velocities to so-called proper-time velocities, which are unbounded. The Newton update is then calculated for the proper-time velocities and the updated proper-time-velocities are mapped back to time–velocity.

To do this, instead of taking the derivative of each position respect to time, we consider the derivative respect to a monotonically increasing proper-time parameter τ_k defined along each orbit by

$$\frac{d\tau_k}{dt_k} \equiv \sqrt{1 - \left|\frac{d\mathbf{x}_k}{dt_k}\right|^2}. \tag{32}$$

From (32) we can derive relations between the two velocities, yielding

$$\mathbf{v}_{k\tau} = \frac{\mathbf{v}_{kt}}{\sqrt{1 - |\mathbf{v}_{kt}|^2}}, \qquad \mathbf{v}_{kt} = \frac{\mathbf{v}_{k\tau}}{\sqrt{1 + |\mathbf{v}_{k\tau}|^2}} \tag{33}$$

where $\mathbf{v}_{kt} \equiv d\mathbf{x}_k/dt_k$, $\mathbf{v}_{k\tau} \equiv d\mathbf{x}_k/d\tau_k$, and notice that proper-time velocities $\mathbf{v}_{k\tau}$ are unbounded, while the velocity $|\mathbf{v}_{kt}| < 1$. The relations between the linear variations of $\mathbf{v}_{kt}$ and $\mathbf{v}_{k\tau}$, as derived from (33) are

$$\Delta\mathbf{v}_{kt} = \frac{\Delta\mathbf{v}_{k\tau}}{\sqrt{1 + |\mathbf{v}_{k\tau}|^2}} - \frac{(\Delta\mathbf{v}_{k\tau} \cdot \mathbf{v}_{k\tau})\mathbf{v}_{k\tau}}{(1 + |\mathbf{v}_{k\tau}|^2)^{3/2}}, \qquad \Delta\mathbf{v}_{k\tau} = (1 + |\mathbf{v}_{k\tau}|^2)^{3/2}(I + \mathbf{v}_{kt}^\dagger \mathbf{v}_{kt})\Delta\mathbf{v}_{kt}. \tag{34}$$

The $\Delta\mathbf{v}_{k\tau}$ calculated from Eq. (34) can be arbitrarily large, which is harmless when added to the *unbounded* $\mathbf{v}_{k\tau}$. Our regularized Newton method updates $\mathbf{v}_{k\tau}$ and only then calculates $\mathbf{v}_{kt}$ using (33), and hence returning a velocity vector of modulus less than one, as required. This avoids the creation of spurious superluminal velocities in the iterative stage, which halt the iteration.

Once we have found trajectories $\boldsymbol{x}_1^h(t_1)$ and $\boldsymbol{x}_2^h(t_2)$ which solve ((29)–(30)), for given boundary data, we need to check that the boundary segment data (a) and (b) satisfy the velocity splicing conditions (c). If there is a velocity discontinuity between the boundary data and the trajectories at $t_1 = t_{L^-}$ or $t_2 = t_{O^+}$, then, as explained in Section 2 the computed solution is invalid. If such velocity discontinuities are detected, we attempt to remove the discontinuities by iteratively redefining the boundary segment data. We redefine the boundary segment of particle 1 so that: (i) the right-derivative becomes equal to $\mathbf{v}_{1,M_1}^h$, and (ii) the points $\mathbf{L}^-$ and $\mathbf{L}^+$ remain unchanged. The adjustment is done by adding to the 3-space components of the boundary segment a function with $\mathbf{Q}(t_1) : [t_{L^-}, t_{L^+}] \to \mathbb{R}^3$, where $\mathbf{Q}(t_1) = (Q^1(t_1), Q^2(t_1), Q^3(t_1))$, and where each component $Q^l(t_1)$ is a polynomial of degree 3. The function $\mathbf{Q}(t_1)$ is determined uniquely by requiring the conditions

(i) and (ii) above, and choosing $\ddot{\mathbf{Q}}(t_{L^+}) = 0$. Boundary segment 2 is analogously redefined between points $\mathbf{O}^-$ and $\mathbf{O}^+$ so that its left-derivative at $\mathbf{O}^+$ is equal to $\mathbf{v}^h_{2,1}$ (the points $\mathbf{O}^-$ and $\mathbf{O}^+$ remain unchanged and the acceleration of boundary segment remains the same at $\mathbf{O}^-$). Using the redefined boundary segments, we resolve equations (29)–(30) with Newton's method using the previously computed numerical solution as the initial guess. We iterate the boundary segment adjustment followed by a Newton method iteration until the velocity discontinuity becomes smaller than the desired tolerance. In our numerical experiments, we observe that velocity discontinuities reduce by approximately two orders of magnitude at each iteration with Newton's method requiring one or two steps per boundary iteration. We also observed that the numerically calculated trajectories are more sensitive to the position of endpoints, $\mathbf{O}_A$, $\mathbf{L}^-$, $\mathbf{O}^+$ and $\mathbf{L}_B$, than to boundary segments of trajectories defined between the points $\mathbf{O}^-$, $\mathbf{O}^+$, $\mathbf{L}^-$ and $\mathbf{L}^+$.

4. Numerically calculated orbits

Now we apply the method detailed in the previous sections to numerically compute solutions of the WFEs of motion with different sets of boundary data. We divide the numerically calculated orbits into two groups of experiments: Experiments I through IV refer to Schild circular orbits, Experiments V through VII refer to other boundary conditions. Until now, the circular orbits were the only known non-colinear solutions of the WFEs, Experiments V–VII demonstrate novel solutions.

In Experiments I–IV, we start with boundary conditions (a) and (b) as segments of a circular orbit. The purpose is twofold: to verify the accuracy of the method, and to explore the basin of attraction of the Newton iteration with respect to the initially guessed trajectories. We find that our integrator can recover the planar solutions of the two-body equations, even starting from non-planar initial guesses with velocities far from the solution velocity. The convergence of the Newton iteration to the circular orbits from strongly perturbed initial conditions is indicative of the circular orbits being an isolated, possibly unique, critical point of the functional S.

In Experiments V–VII, we explore new solutions when the boundary conditions are close to circular orbits. The boundary data corresponds to part of a spiral trajectory obtained by perturbing two nearby circular orbits. The initially guessed solution is the completion of the spiral trajectory between the boundary data. Depending on the radial difference in the boundary conditions and the length of the trajectory, we find qualitatively different solutions: in Experiment V we find the solution is indeed a spiral, in Experiment VI we find the solution closes onto itself (but not in a periodic way), and in Experiment VII we find the solution is far from circular. We also discuss an interpretation of these experimenters with respect to the convexity of the functional and the existence of a bifurcation.

We remark that for Experiments V–VII, the iterative boundary adjustment described in Section 3 needs to be undertaken. The Newton regularization, also described in Section 3, was needed only for Experiment VII, whose solution is far from the initially guessed solution. Without regularization the Newton updates for this problem results in superluminal orbits and the method fails. For Experiments I–VI the Newton iteration converges to the same solution with or without regularization.

In all experiments we specify boundary conditions (a) and (b) as above, and an initial guess for the corresponding solution $(\boldsymbol{x}_1(t_1), \boldsymbol{x}_2(t_2))$ of ((22)–(23)). We apply our finite element method as detailed in Section 3 to solve ((29)–(30)) in $N_h(\boldsymbol{x}_{1L}, \boldsymbol{x}_{2L})$ using Newton's method, iterating until the gradient essentially vanishes within the machine precision, namely, $\|\nabla_h S(\mathbf{x}^h_1, \mathbf{x}^h_2)\|_\infty \leq 10^{-10}$.

In Experiments I–IV, we use boundary data corresponding to the known Schönberg–Schild circular-orbit solutions [5, 6] in the plane. In these solutions, two particles rotate at constant speed in diametrical opposition on circular orbits (of different radii, unless the masses are equal). A particle at time t interacts with the other particle in future and past, with the future and past positions both at *delay angle* θ to the common diameter (see Fig. 2). Boundary conditions are chosen so that the circular orbits lie in the xy-plane, but we emphasize that the numerical algorithm works with three space dimensions, and as a test for the algorithm we deliberately choose an initial guess for the solution which is not planar.

Experiment I uses planar boundary data extracted from the circular-orbit solution for $m_1 = 1$ and $m_2 = 2$ with retardation angle $\theta = 0.1$ and $t_{L_B} - t_{O_A}$ equal to one quarter of the circular period. We deliberately start with an initial guess for the orbit which is far from circular or planar motion, and use a modulated solenoid as illustrated in Fig. 3(i) to seed the Newton iteration. The modulated solenoid used has maximum particle velocity 0.30775 for particle 1, whereas on the underlying circular orbit particle 1 has speed 0.066740, so the seed function is far from the circular orbit in functional space, even though it is wrapped tightly around the circular orbit in physical space.

We divided the orbit of particle 1 into $N = 400$ parts and that of particle 2 into 401 parts. Since the exact motion is circular of constant speed if both trajectories are divided into an equal number of parts then for the exact solution the light-cones of the mesh points fall exactly on the mesh points of the other particle trajectory, while for the numerical solution the mesh points will be in light-cone condition up to numerical precision creating either some very short quadrature intervals or (if the light-cones numerically cross each other) an inconsistent ordering of quadrature-endpoints in (31). Although the numerical code can catch these exceptional events (consuming additional computational time), they are avoided altogether by perturbing the grid spacing.

The mesh results in a band-diagonal 4818×4818 Jacobian matrix with 0.7% nonzero elements to construct for each Newton iteration. The Newton method converged in 9 iterations to the circular orbit, as illustrated in Fig. 3(ii). Notice that even though the accelerations were allowed to be discontinuous, the minimization converged quickly to a C^1 circular orbit. The absolute and relative errors for the computed particle positions and velocities is shown in Table 1. The velocity at the

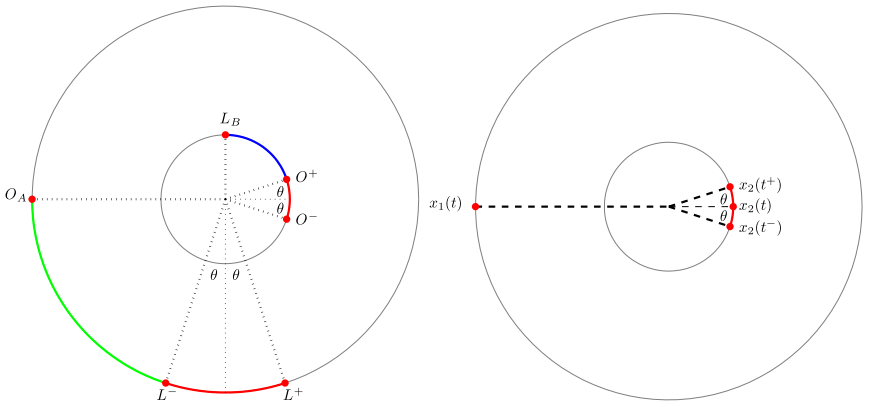


Fig. 2. (i) A Schönberg–Schild circular orbit $(\boldsymbol{x}_1(t_1), \boldsymbol{x}_1(t_2))$ for $t_1 \in [t_{O_A}, t_{L^-}]$ and $t_2 \in [t_{O^+}, t_{L_B}]$ and the boundary conditions which consist of (a) the initial point $O_A = \boldsymbol{x}_1(t_{O_A})$ of the trajectory $\boldsymbol{x}_1(t_1)$ of particle 1 and the boundary segment $\boldsymbol{x}_2(t_2)$ for $t_2 \in [t_{O^-}, t_{O^+}]$ of particle 2 inside the light-cone of O_A, and (b) the final point $L_B = \boldsymbol{x}_2(t_{L_B})$ of the trajectory of particle 2 and the boundary segment $\boldsymbol{x}_1(t_1)$ for $t_1 \in [t_{L^-}, t_{L^+}]$ of particle 1 inside the light-cone of L_B. (ii) A snapshot of the solution highlighting the delay angle θ; although the particles rotate at constant speed in diametrical opposition on circles with a common center, particle 1 at time t interacts with particle 2 in the advanced and retarded light-cones at t^+ and t^-.

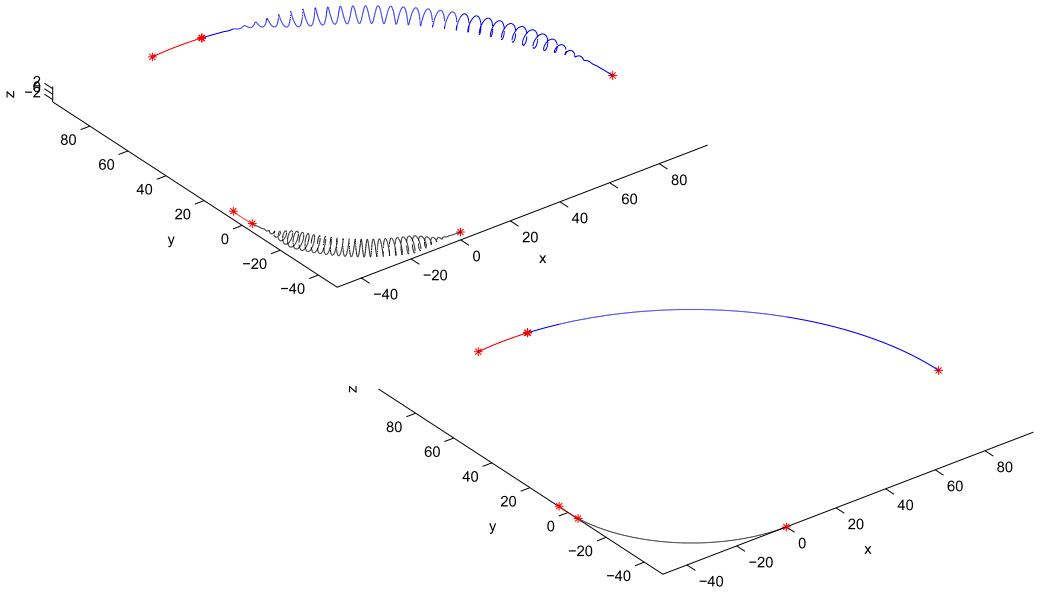


Fig. 3. (i) Boundary data and initial trajectories for Experiment I based on a $\pi/2$ arc of circular-orbit solution with retardation angle $\theta = 0.1$ for $m_1 = 1$ and $m_2 = 2$. The initial trajectory of particle 1 has a modulated solenoidal motion (blue) superposed to the guiding circle for an arc of $\pi/2 - \theta$ and ending on the circular boundary data (red). Trajectory 2 starts from the circular boundary data segment for an arc of θ (red) merged to an initial motion given by a solenoid (black) superposed on the circular orbit. (ii) Converged Newton iteration for Experiment I is a circular orbit for particle 1 (solid blue) and a circular orbit for particle 2 (solid black), falling exactly on the circular solution with retardation angle $\theta = 0.1$ for $m_1 = 1$ and $m_2 = 2$. (For interpretation of the references to colour in this figure legend, the reader is referred to the web version of this article.)

Table 1
Absolute and Relative Errors for the computed position and velocities for Experiment I as the mesh is refined.

N	$\sup \|\mathbf{x}^h - \mathbf{x}\|$	$\sup \left(\frac{\|\mathbf{x}^h - \mathbf{x}\|}{\|\mathbf{x}\|}\right)$	$\sup \|\dot{\mathbf{x}}^h - \dot{\mathbf{x}}\|$	$\sup \left(\frac{\|\dot{\mathbf{x}}^h - \dot{\mathbf{x}}\|}{\|\dot{\mathbf{x}}\|}\right)$
25	1.96e−5	1.97e−7	8.10e−7	1.21e−5
50	2.96e−6	2.97e−8	8.09e−7	1.21e−5
100	8.30e−7	8.34e−9	3.99e−7	5.99e−6
200	3.15e−7	3.17e−9	9.13e−8	1.36e−6
400	8.27e−8	8.31e−10	6.07e−8	9.10e−7
800	1.04e−7	1.05e−9	5.54e−8	8.30e−7

boundary points O^+ and L^- was found to be continuous up to numerical precision even though this was not enforced in the code (discontinuities of magnitude 1.6718×10^{-7} and 7.1725×10^{-8} were detected at L^- and O^+ respectively).

To test the convergence of the method we used successive refinements of the time-grid in Experiment I, with $N = 25$, 50, 100, 200, 400, and 800 and measured the errors of the computed solutions with respect to the known exact solution. The errors are reported in Table 1. We see that the grid $N = 400$ is already close to the optimal refinement; with one more refinement of the grid to $N = 800$, the relative error in position actually increases. As in any integration method, there is a trade-off between reduction in "truncation errors" and increase in round-off errors; in our case the "time-stepping" is determined by the grid of the quadrature rule which is chosen to have at least $24 \times N$ points along each trajectory.

Assuming the error scales as N^{-p} between the $N = 25$ and $N = 400$ grids we obtain a convergence order of $p = \log(1.97/0.00831)/\log(16) = 1.97$ for the relative position error and $p = 0.93$ for the relative velocity error. When measuring the relative errors in the L^1 we find similar results, the numerical order of convergence is 2.09 for the position and 0.94 for the velocity respectively.

These convergence rates (approximately order 2 for the position and order 1 for the velocity) are to be expected in general. Noting that the exact solution of (22), (23) in $N(\boldsymbol{x}_{1L}, \boldsymbol{x}_{2L})$ is in general a C^1 trajectory which is piecewise C^2 with second order derivative defined almost everywhere, and that the Hermite interpolant of this exact solution on the numerical time-grid is itself a function in the finite element space $N_h(\boldsymbol{x}_{1L}, \boldsymbol{x}_{2L})$, which can be shown to be order 2 for the position and order 1 for the velocity, the "best" approximation in $N_h(\boldsymbol{x}_{1L}, \boldsymbol{x}_{2L})$ to the solution in $N(\boldsymbol{x}_{1L}, \boldsymbol{x}_{2L})$ must therefore be at least this accurate. This expected accuracy justifies other choices in the construction of the algorithm, in particular the choice of the second order Composite Trapezoidal rule to evaluate integrals (29) and (30). However, we note that the use of second order centered finite differences in evaluating the entries in the Jacobian matrix does not affect the accuracy of the solution since we always solve until the residual satisfies $\|\nabla_h S(\mathbf{x}_1^h, \mathbf{x}_2^h)\|_\infty \leq 10^{-10}$, though it could affect the convergence rate of Newton's method to this solution. In the particular case of Experiment I, the underlying solution is C^∞, and as noted in the discussion of the numerical method, in that case interpolating the exact solution in $N_h(\boldsymbol{x}_{1L}, \boldsymbol{x}_{2L})$ would give fourth order convergence in position and third order in velocity. That we do not see such convergence rates in the numerical experiment is likely due to the implementation of the finite element method being tailored to the less regular general case.

In Experiment II, we double the time interval of Experiment I so that $t_{L_B} - t_{O_A}$ is equal to half the circular period, but we leave the masses and retardation angle unchanged. We again use a mesh of 400 and 401 points for each particle, so since $t_{L_B} - t_{O_A}$ has been doubled from Experiment I, the grid is twice as coarse in Experiment II. We again found that the Newton iteration converged in 9 iterations from the modulated Solenoid seed to the circular orbit (we omit the figures since they are very similar to Figs. 3 and 4). The computed orbit had a relative error of 1.24×10^{-9} in the computed maximum particle velocity compared to the circular orbit. We again found the velocities to be continuous up to numerical precision, with numerical discontinuities of magnitude 1.7794×10^{-7} and 8.8996×10^{-8} detected in the velocities at L^- and O^+ respectively, which is only fractionally larger than in the previous example.

We find by inspection that the numerical Jacobian matrix at the solution is positive definite in both Experiment I and II with eigenvalues in the range $[9.3857 \times 10^{-6}, 3.6357]$ for Experiment I and $[4.1969 \times 10^{-7}, 7.5372]$ for Experiment II, with the condition number of the matrix rising from 3.8×10^5 to 1.8×10^7. It is shown in [17] that for sufficiently large radii the circular-orbit solution is a local minimum of the functional which implies that the Hessian of the functional is positive definite. Since the Jacobian matrix used in Newton's method is a discretization of this Hessian, the positive definiteness of the computed Jacobian is an indication of this. We remark that the goal in approximating the Hessian is to guide the Newton iteration to a critical point, albeit a saddle, rather then precisely approximating the second functional derivative. Nevertheless, the eigenvalues of the computed Jacobian can indicate the type of critical point or, as in Experiments I and II, they can indicate a trend. The errors in the computed Jacobian, $\tilde{\nabla}_h^2 S$, can be inferred from its skew-symmetric part (the columns of the computed Jacobian are computed independently; see Section 3). In Experiment I, the matrix 2-norm of the skew-symmetric part is 3.9×10^{-3} which is small when compared with the norm of the symmetric part: 3.6357. We can also infer how the numerical errors influence the eigenvalues in Experiment I. The absolute difference between the largest eigenvalues of $\tilde{\nabla}_h^2 S$ and of its symmetric part is 1.2×10^{-9}, the difference between the smallest eigenvalues is 2.0×10^{-9}, the error appears to be limited by an absolute precision less then 10^{-8}. A direct computation of the exact eigenvalues would require explicit formulas for the Hessian, a formidable task.

The boundary data and initial seed orbits for Experiment III are illustrated in Fig. 4(i). The boundary data uses a segment of the circular-orbit solution with retardation angle $\theta = 0.05$ and $t_{L_B} - t_{O_A}$ equal to 3/4 of the circular period, while the initial seed orbits superimpose a solenoidal motion onto the circular orbit. Again Newton's method converged to an arc of circular orbit (in 7 iterations) with continuous velocity and acceleration to numerical precision (numerical velocity discontinuities at O^+ and L^- where respectively 2.2534×10^{-7} and 1.1324×10^{-7}), as illustrated in Fig. 4(ii). The Hessian at the final solution has a single negative eigenvalue; -5.9517×10^{-7}. However, this is of order of the numerical tolerance from zero, and so it is not possible to draw a definitive conclusion on the definiteness of the Hessian matrix.

For Experiment IV, the boundary data and initial seed trajectories are similar to the previous examples, but now with retardation angle $\theta = 0.1$ and time $t_{L_B} - t_{O_A}$ equal to the circular period. The method again converges to a circular orbit, (not illustrated), with continuous velocity and acceleration to numerical precision (numerical velocity discontinuities at O^+ and L^- were respectively 1.4665×10^{-7} and 4.1731×10^{-8}). But again we cannot determine whether the Hessian at the solution is positive definite (the numerical Hessian has one negative eigenvalue -9.9475×10^{-7} of order of the numerical precision and 4811 positive eigenvalues ranging between 4.1731×10^{-8} and 15.3218).

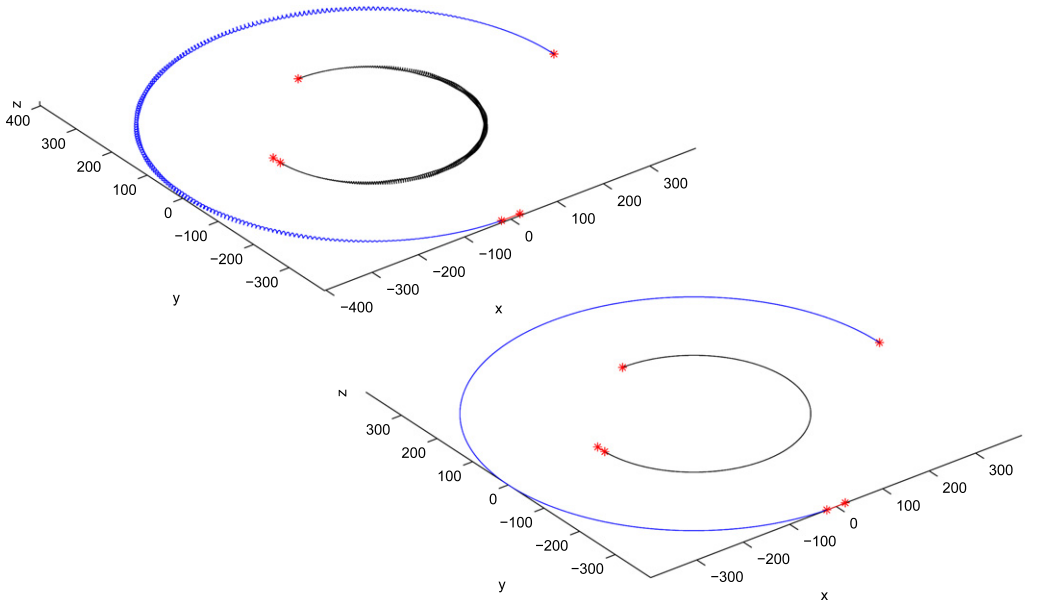


Fig. 4. (i) Boundary data for Experiment III based on a $3\pi/2$ arc of circular-orbit solution with retardation angle $\theta = 0.05$ for $m_1 = 1$ and $m_2 = 2$. The initial seed trajectory of particle 1 has a modulated solenoidal motion (blue) superposed onto the guiding circle for an arc of $3\pi/2 - \theta$ and ending on the circular boundary data (red). Trajectory 2 starts from the circular boundary data segment for an arc of θ (red) and continues as a modulated solenoidal motion (black) superposed to the circular orbit. (ii) Converged Newton iteration for Experiment III is a circular orbit for particle 1 (solid blue) and a circular orbit for particle 2 (solid black), falling on the known circular solution. (For interpretation of the references to colour in this figure legend, the reader is referred to the web version of this article.)

Experiments I–IV show that our integrator can accurately recover the circular-orbit solutions even starting from initial guesses with a large perturbation from the exact solution, as in the case of the modulated solenoid initial conditions. This indicates that the circular orbits correspond to a probably isolated, and possibly unique, critical point of the functional S. The circular orbits are probably convex critical points but, by comparing Experiments I and II, there is an indication that the convexity weakens as the segment of the trajectory increases in length. For asymptotically large radius, the circular orbits are local minimum points [17] but this assertion does not preclude the existence of saddle points in our numerical experiments.

In the remaining experiments, we attempt to produce novel planar spiral trajectories. The spiral boundary conditions and proto-orbit were created using two nearby circular orbits, with the spiral rotation speed taken to be the average of the two circular rotation frequencies. The radii were varied using an exponential law so that the spiral orbit crosses the first circular orbit at $t = t_{O_A}$ and the second circular orbit at $t = t_{L_B}$. The boundary segments thus created lie on planar spirals (and not on circular orbits).

In Experiment V, we took a spiral boundary data and proto-solution based on two circular orbits with $m_1 = 1, m_2 = 2$ and delay angles $\theta = 0.1$ and $\theta = 0.09$, which results in the radii of the orbits increasing by a factor of $(0.1/0.09)^2$ between t_{O_A} and t_{L_B}. Taking $t_{L_B} - t_{O_A}$ to be equal to $1/2$ of the spiral period, gives spiral boundary data and proto-solution as illustrated in Fig. 5(i). The Newton method initially converged to a solution with velocity discontinuities of 0.0092602 at O^+ and 0.018888 at L^- (see Fig. 6(i)), so the given boundary data did not satisfy the splicing condition (c). Adapting the boundary data as detailed in Section 3, results in the solution illustrated in Fig. 5(ii) which has continuous velocity (see Fig. 6(ii) where numerical velocity discontinuities have been reduced to 10^{-10}). The boundary adaptation appears to have little effect on the solution within the computational domain; the solution with the unadapted boundary data was visually identical to the adapted boundary data solution shown in Fig. 6(ii).

Fig. 7(i) shows the acceleration of particle 1 over the computational domain. There is clearly a relatively large discontinuity in the acceleration at $t = t_{L^-}$, which is not surprising since continuity of the acceleration is neither needed nor enforced in our treatment. Although the solution appears to have continuous acceleration within the computational interval, Fig. 7(ii) which is a zoomed view of a part of Fig. 7(i) clearly shows that the acceleration is in general discontinuous at the mesh points. These discontinuities are very small, with the largest being seen on the trajectory of particle 1 at the time point that falls in the forward light-cone of O^+ (as occurs in Fig. 7(ii)) and at the point of the trajectory of particle 2 that falls in the backward light-cone of L^-. The discontinuous nature of the acceleration is not an artifact of the numerical discretization. Discontinuous acceleration at breaking points even for C^2 data is to be expected, as a neutral-delay equation can propagate discontinuities [24,28]. In our two-body problem these breaking points form a sewing chain of points in light-cone condition alternating between the two trajectories starting at the boundary points O^+ and L^-.

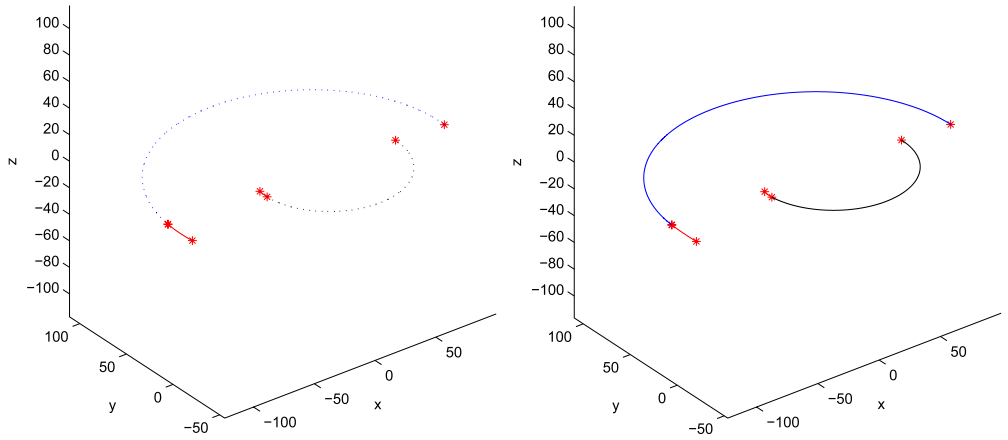


Fig. 5. (i) Boundary data for Experiment V: half a period of an exponential spiral solution with $m_1 = 1$ and $m_2 = 2$ and radius increasing by a factor of $(0.1/0.09)^2$ over the half period. The initial seed trajectories are the same monotonic spirals (broken lines) connecting the boundary data. (ii) Converged Newton iteration for Experiment V with adapted history is a monotonic spiral as guessed.

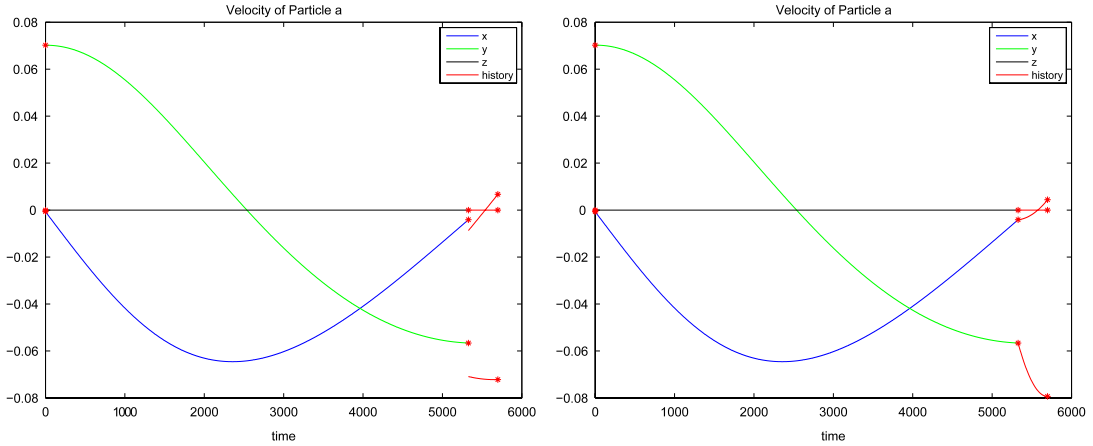


Fig. 6. Converged solution for Experiment V. Illustrated is the velocity of particle 1, which is seen to be (i) discontinuous at L^-, with the initially given history, but (ii) continuous after adaptation of the history.

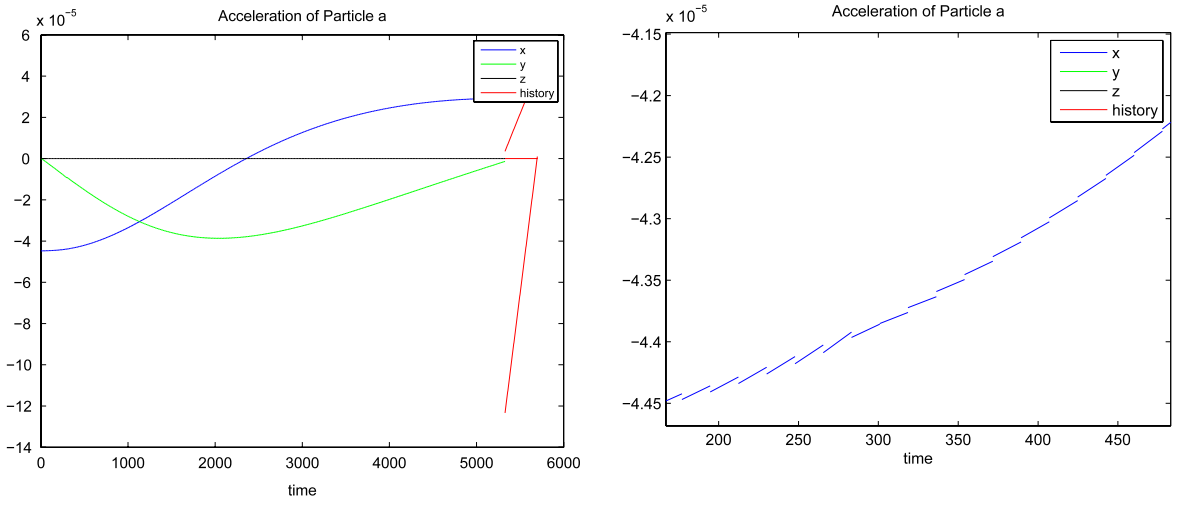


Fig. 7. Converged solution for Experiment V with adapted history: illustrated is the acceleration of particle 1, which is seen (i) to be discontinuous at L^- and (ii) on the zoomed detail is seen to have very small discontinuities of order of 1×10^{-7} at the computational mesh points.

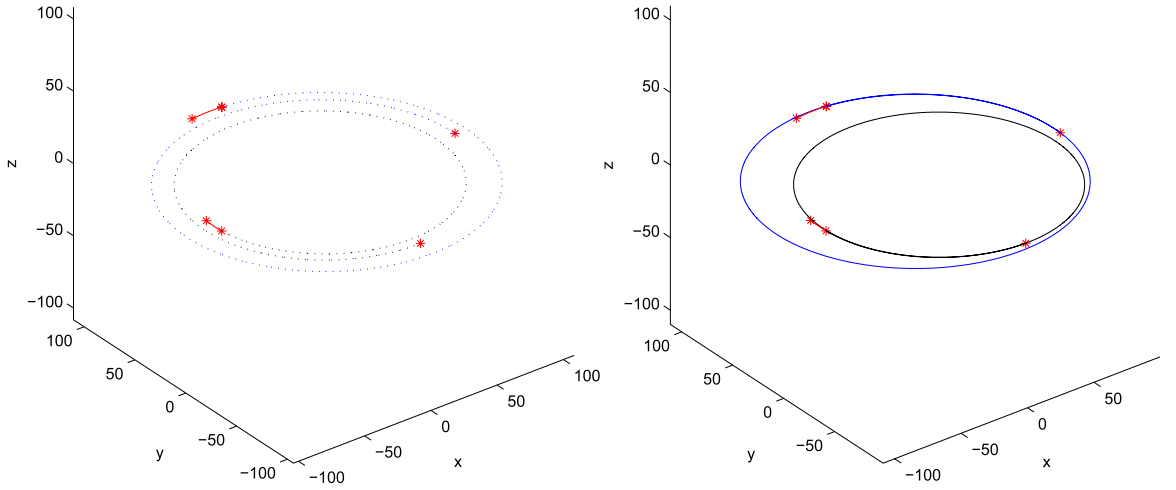


Fig. 8. Boundary data for Experiment VI: 5/4 of a period of an exponential spiral solution with $m_1 = 1$ and $m_2 = 1.2$ and radius increasing by a factor of $(1/0.95)^2$ over the time interval $t_{L_B} - t_{O_A}$. (i) The seed trajectories are monotonic spirals (broken lines) connecting the endpoints. (ii) The converged solution with adapted history is not a monotonic spiral, but neither is it quite periodic.

The numerically calculated Hessian in Experiment V evaluated on the computed orbit was positive definite with smallest eigenvalue 2.3618×10^{-7}, indicating the orbit could correspond to a minimum of the functional S. The variational theory of local Lagrangians [29] says that an orbit is a minimum whenever there is a unique solution to the variational equations. The minimality property is no longer granted at bifurcations where typically conjugate points appear and two or more solutions exist for the variational equations. The loss of minimality is sought in Experiment VI which again attempted to produce a spiral, this time based on two circular orbits with $m_1 = 1, m_2 = 1.2$ and delay angles $\theta = 0.1$ and $\theta = 0.095$, which results in the radii of the orbits increasing by a factor of $(1/0.95)^2$ between t_{O_A} and t_{L_B}. Taking $t_{L_B} - t_{O_A}$ equal to 5/4 of the spiral period, gives the spiral boundary data and proto-solution as illustrated in Fig. 8(i). Newton's method converged in 13 iterations, with residuals not decreasing monotonically until after the sixth iteration, indicating that the initial spiral seed orbit was far from a solution. The solution found again had velocity discontinuities at O^+ and L^- (of magnitudes 0.0072176 and 0.0060321), indicating that the given boundary data did not satisfy the splicing condition (c). Two steps of boundary adaptation, requiring a total of 6 additional Newton steps resulted in the continuous solution shown in Fig. 8(ii) (where numerical velocity discontinuities have again been reduced below 10^{-10}). The solution with the unadapted boundary data is not shown, as visually it is indistinguishable from Fig. 8(ii). The solution found is clearly not close to the spiral orbit postulated, indicating that our method can be applied in cases where the solution is not already known. Fig. 8(ii) suggests that the orbits may be periodic, but this is not so. Since a bounded periodic orbit can be extended to infinite negative and positive time, the boundary segments of trajectory would need to agree with the computed orbit n periods later or earlier. But, in Fig. 9(ii) we see that while the velocity is continuous for the adapted boundary data, it is not periodic. Fig. 9(i) shows clearly that without boundary adaptation the splicing condition (c) is violated.

The Hessian evaluated at the orbit of Experiment VI was no longer positive-definite, having a smallest eigenvalue of -9.6688×10^{-6}, suggesting that a conjugate point and therefore another critical orbit exists for the same boundary data.

Fig. 10(i) shows the acceleration of particle 1 over the computational domain. There is again a relatively large discontinuity in the acceleration at $t = t_{L^-}$, while Fig. 10(ii) reveals very small discontinuities in the acceleration at mesh points.

The loss of minimality is clearly illustrated in Experiment VII which again attempted to produce a spiral with $m_1 = 1$, $m_2 = 1.2$ and $t_{L_B} - t_{O_A}$ to be equal to 5/4 of the spiral period. The only difference to the previous experiment is that now we take delay angles of $\theta = 0.1$ and $\theta = 0.09$ for the two circular orbits used to define the spiral, which results in the radii of the orbits increasing by a factor of $(1/0.9)^2$ between t_{O_A} and t_{L_B}. The resulting spiral boundary data and proto-solution are illustrated in Fig. 11(i). The numerical method converged to the orbit shown in Fig. 11(ii) which is completely different from the postulated solution. The Newton method required 20 iterations to converge to the trajectories shown in Fig. 12(i) which clearly have velocity discontinuities at the history segment boundaries, and two steps of boundary adaptation requiring another 8 Newton iterations to produce the C^1 solution shown Fig. 12(ii). We see from Fig. 12 that adapting the boundary data has little discernible effect on the solution inside the computational interval.

Fig. 13 shows the acceleration of particle 1 over the computational domain. There is again a relatively large discontinuity in the acceleration at $t = t_{L^-}$, while Fig. 13(ii) reveals very small acceleration discontinuities at the mesh points, with the most significant near the beginning of the computational interval (in light-cone condition with O^+). As noted previously, the neutrality of the equations allows the discontinuities in the acceleration at the boundary points to propagate into the computational domain on a chain of breaking points. Here we see numerical evidence of the first such breaking point.

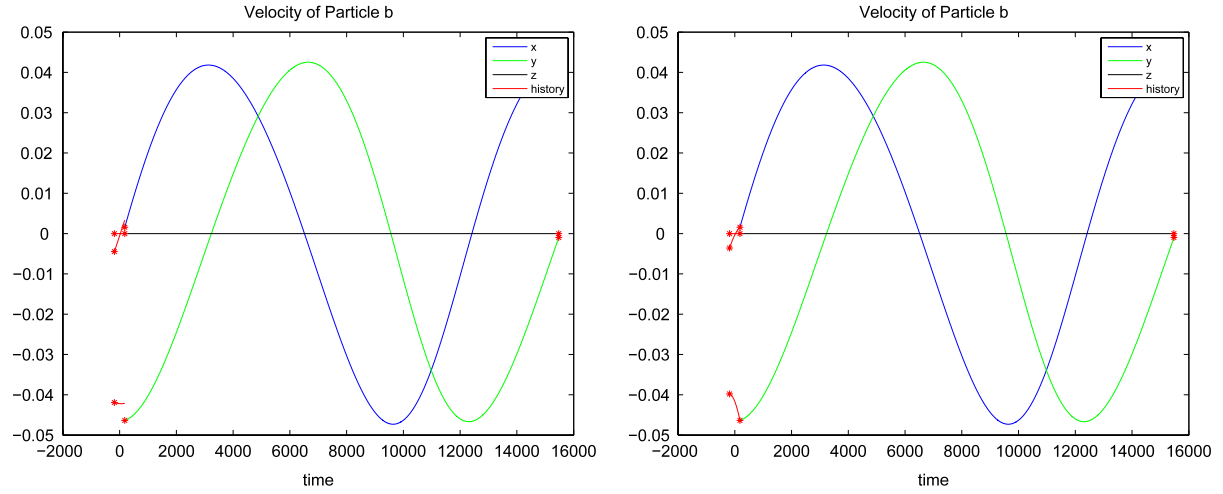


Fig. 9. Converged solution for Experiment VI. Illustrated is the velocity of particle 2, which (i) for the initially given boundary data is seen to be discontinuous at O^+, and (ii) for the adapted boundary data is seen to be continuous.

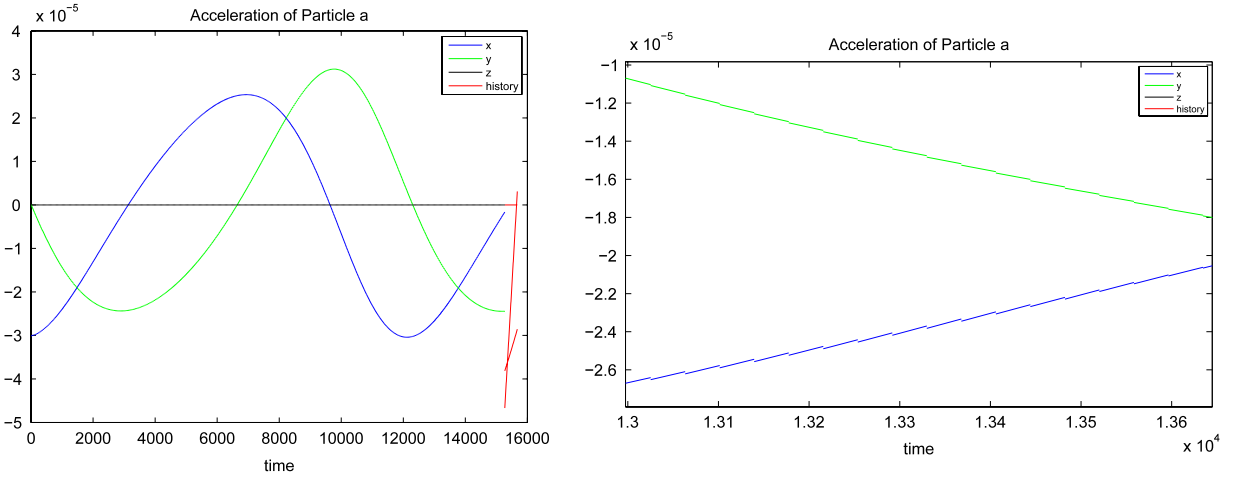


Fig. 10. Converged numerical solution for Experiment VI with adapted history. Illustrated is (i) the acceleration of particle 1, which is seen to be discontinuous at L^- and (ii) a zoomed detail of the acceleration showing the small discontinuities at the mesh points.

The numerically computed Hessian evaluated on the converged orbit for Experiment VII is positive-definite, (with smallest eigenvalue 6.0354×10^{-7}), suggesting that a new minimum was created in a bifurcation somewhere.

5. Discussions and conclusion

The WFEs have been an active area of study since the 1940s, however, little headway had previously been made on finding solutions of the full equations, except in some very special cases. In this work we have developed a boundary value numerical integrator for the electromagnetic two-body problem, which allows us to compute solutions of the full WFEs on finite time segments for the first time.

This allowed us to investigate new types of orbits close to the circular-orbit solutions and to study nontrivial dynamics.

We formulate the problem using a finite action (based on the Fokker action) with suitably defined boundary conditions where boundary points and boundary segments are given, Fig. 1. The Wheeler–Feynman equations of motion for the two-body problem follow from the critical-point condition of this functional S. These neutral state-dependent advanced-delay equations pose a major computational and theoretical challenge because a state-dependent neutral differential-delay equation may not regularize the solution at subsequent breaking points, furthermore, the positions of the breaking points are not known *a priori*. We sought solutions of the Wheeler–Feynman equations with C^1 regularity because, with this low regularity, the equations are everywhere equivalent to the critical-point condition of the action functional S. To guarantee the solution is indeed C^1 we need to enforce an implicit boundary condition, called a splicing condition, where the boundary segment must match continuously with the position and velocity of the trajectory at boundary-points.

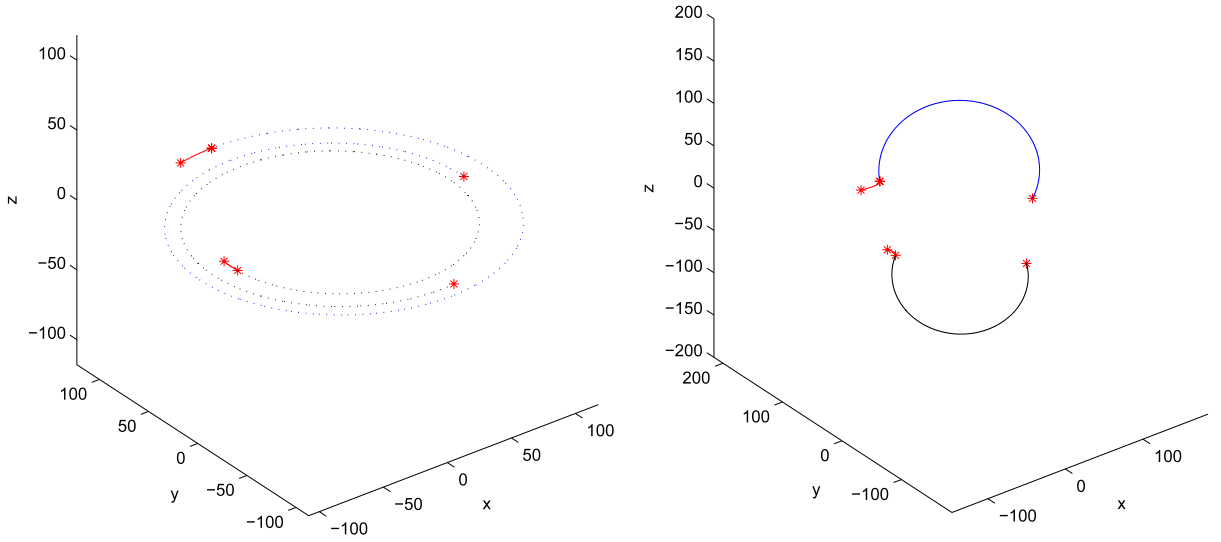


Fig. 11. (i) Boundary data for Experiment VII: 5/4 of a period of an exponential spiral solution with $m_1 = 1$ and $m_2 = 1.2$ and radius increasing by a factor of $(1/0.9)^2$ over the time interval $t_{L_B} - t_{O_A}$. The initial seed trajectories are the same monotonic spirals (broken lines) connecting the boundary data. (ii) Converged numerical solution for Experiment VII with adapted boundary data. The orbit *is* planar and has continuous velocity, but is clearly very different from the guessed spiral.

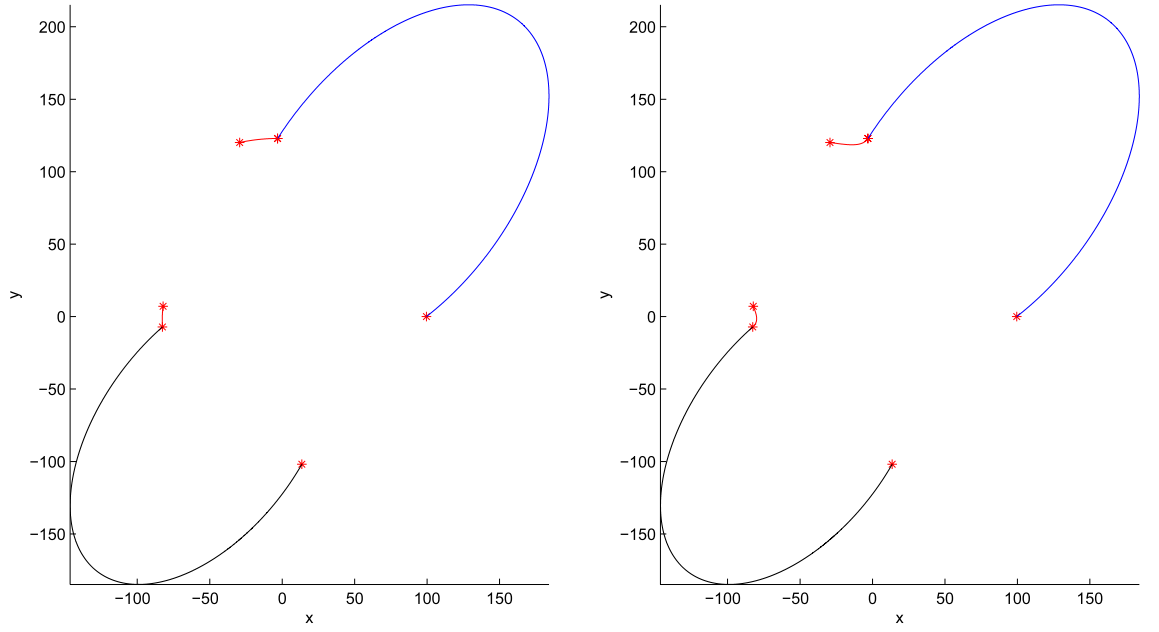


Fig. 12. Converged solutions for Experiment VII. Since the orbits are planar, we only show the solutions in the *xy*-plane. (i) The solution for the given boundary data has discontinuous velocity at t_{O^+} and t_{L^-}, and so is not valid as a solution of the variational problem. (ii) The solution with adapted boundary data. The six points $\mathbf{x}_1(t_{O_A})$, $\mathbf{x}_2(t_{L_B})$, $\mathbf{x}_1(t_{L^\pm})$ and $\mathbf{x}_2(t_{O^\pm})$ are held fixed by the adaptation, and only the two history segments for $t_1 \in [t_{L^-}, t_{L^+}]$ and $t_2 \in [t_{O^-}, t_{O^+}]$ are varied. Notice that the solution over the computational interval varies very little when the boundary data is adapted.

To computationally solve the Wheeler–Feynman equations, we developed a Finite Element method based on the variational formulation using C^1 basis functions. A standard Newton method with approximate Jacobian was used to seek the critical point (possibly a saddle point). We used an iterative adjustment of the boundary segment to the computed trajectory until the splicing condition was satisfied. The iterative adjustment was seen to converge quickly because the solutions we computed show low sensitivity to changes in the boundary segment.

In numerical experiments, we showed that our method can recover the known circular-orbit solutions and used these solutions to test the convergence of our method, finding second order convergence in the spatial variables and first order convergence in the velocity variables. Further numerical experiments with the circular-orbit solution have shown that it is a strong attracting critical point of the action, i.e., it has a large basin of attraction when using the Newton method. This

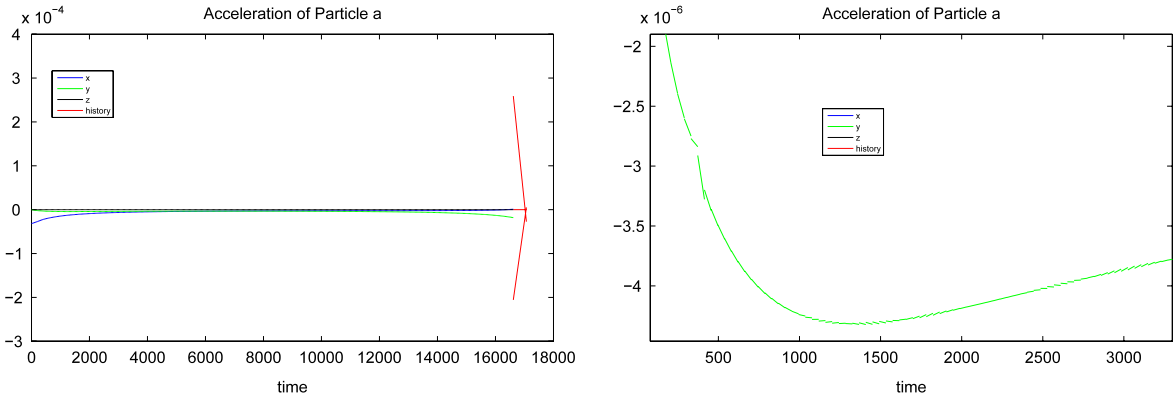


Fig. 13. Converged solution for Experiment VII with adapted history. Illustrated is the acceleration of particle 1, which is seen in (i) to be discontinuous at t_{L^-} and in (ii) a zoom of the detail shows it to have very small discontinuities at the mesh points, with the largest (still small) discontinuity where the solution is in light-cone condition with O^+.

finding is further supported by theoretical estimates that the circular orbit is a local minimum of the action for large enough radius.

By perturbing the endpoints and boundary segments of circular orbits we found completely new trajectories with various behaviors. The trajectories were found to be much more sensitive to perturbations in the space–time positions of the boundary-points than to perturbations in the boundary segments. We devised experiments where the initial guess is a spiral trajectory connecting two near by circular orbits with different radial parameters. For short trajectories we indeed find spiral-like solutions, Fig. 5, for medium length trajectories we found almost-circular non-concentric trajectories, Fig. 8, and for longer trajectories the Newton method converged to a completely different type of trajectory where particles are driven in opposing parabolic-like trajectories, Fig. 12. This indicates that spiral trajectories, when they exist, become less attractive critical points to the Newton method as the length of the trajectory increases.

We verified numerically that acceleration jumps, although small, indeed exist in the numerical solution (Fig. 13). The acceleration jump does not seem to propagate significantly at subsequent breaking points as the worst case scenario would suggest. This unexpected regularization of the acceleration might be a general property of the Wheeler–Feynman equations or a feature of the particular type of orbits we have experimented with, or a feature of our numerical method.

Finally we remark that the electromagnetic two-body problem is a challenging computational problem that is still lacking a complete physical and mathematical understanding. The most prominent feature being the possibility to propagate discontinuities of the derivatives through successive breaking points. Thus, it would be interesting to consider critical points with C^0 regularity (this allows for any C^0 boundary segment to be prescribed). The critical point of the action is then the Wheeler–Feynman equation of motion almost everywhere except at the breaking points where a velocity jump condition must be obeyed [26]. The propagation of velocity discontinuities is certainly more dramatic than acceleration discontinuities and would lead to completely new dynamics.

Acknowledgments

This work was partially supported by CNPQ (Brazil), FAPESP (Brazil) and NSERC (Canada). The authors acknowledge the hospitality and partial support of the Max Planck Institute for the Physics of Complex Systems (Germany). J. De Luca acknowledges discussions with Coraci Malta.

References

[1] K. Schwarzschild, Nachr. Akad. Wiss. Göttingen Math.-Phys. Kl. IIa 126 (1903) 132–245.
[2] H. Tetrode, Z. Phys. 10 (1922) 317;
A.D. Fokker, Z. Phys. 58 (1929) 386;
A.D. Fokker, Physica 9 (1929) 33;
A.D. Fokker, Physica 12 (1932) 145.
[3] J.A. Wheeler, R.P. Feynman, Rev. Modern Phys. 17 (1945) 157; Rev. Modern Phys. 21 (1949) 425.
[4] J.D. Jackson, Classical Electrodynamics, second ed., Wiley, 1975.
[5] M. Schönberg, Phys. Rev. 69 (1946) 211.
[6] A. Schild, Phys. Rev. 131 (1963) 2762.
[7] R.D. Driver, Phys. Rev. D 19 (1979) 1098.
[8] G. Bauer, D.-A. Deckert, D. Durr, 9 August 2011. arXiv:1009.3103v2 [math-ph].
[9] D. Louis-Martinez Junior, Phys. Lett. A 320 (2003) 103; Phys. Lett. B 632 (2006) 733; Phys. Lett. A 364 (2007) 93.
[10] C.M. Andersen, H.C. von Baeyer, Phys. Rev. D 5 (1972) 2470.
[11] J. De Luca, Phys. Rev. E 73 (2006) 026221; Phys. Rev. E 71 (2005) 056210.
[12] E.H. Kerner (Ed.), The Theory of Action-at-a-Distance in Relativistic Particle Dynamics, Gordon and Breach, New York, 1972.
[13] F. Hoyle, J.V. Narlikar, Lectures on Cosmology and Action at a Distance Electrodynamics, World Scientific, London, 1996.

[14] J.L. Kaplan, M. Sorg, J.A. Yorke, Nonlinear Anal. TMA 3 (1979) 53.
[15] J.A. Murdock, Ann. Physics 84 (1974) 432.
[16] R.D. Driver, J. Differential Equations 54 (1984) 73; Nonlinear Anal. 8 (1984) 155.
[17] J. De Luca, J. Math. Phys. 50 (2009) 062701.
[18] E.B. Hollander, J. De Luca, Phys. Rev. E 67 (2003) 026219; Chaos 14 (2004) 1093.
[19] C.K. Raju, J. Phys. A: Math. Gen. 13 (1980) 3303; Found. Phys. 34 (2004) 937.
[20] J. De Luca, N. Guglielmi, A.R. Humphries, A. Politi, J. Phys. A 43 (2010) 205103.
[21] K. Engelborghs, T. Luzyanina, D. Roose, ACM Trans. Math. Softw. 28 (2002) 1.
[22] K.A. Abell, C.E. Elmer, A.R. Humphries, E.S. Van Vleck, SIAM J. Appl. Dyn. Syst. 4 (2005) 755.
[23] J. Stoer, R. Bulirsch, Introduction to Numerical Analysis, third ed., Springer-Verlag, 2002.
[24] A. Bellen, M. Zennaro, Numerical Methods for Delay Differential Equations, OUP, 2003;
A. Bellen, S. Maset, M. Zennaro, N. Guglielmi, Acta Numer. 18 (2009) 1–110.
[25] F. Hartung, T. Krisztin, H.-O. Walther, J. Wu, Functional differential equations with state-dependent delays: theory and applications, in: Handbook of Differential Equations, vol. 3, Elsevier, 2006.
[26] J. De Luca, Phys. Rev. E 82 (2010) 026212.
[27] J. De Luca, Electromagnetic models to complete quantum mechanics, J. Comput. Theory Nanosci. 8 (2011) 1040.
[28] J. Hale, Theory of Functional Differential Equations, Springer-Verlag, 1977.
[29] John L. Troutman, Variational Calculus and Optimal Control: Optimization with Elementary Convexity, second ed., Springer, 1995.